PHYSICAL REVIEW D **96,** 123532 (2017)

Solving the Vlasov equation in two spatial dimensions with the Schrödinger method

Michael Kopp,[1,2,*] Kyriakos Vattis,[1,3,†] and Constantinos Skordis[1,2,‡]

[1]*Department of Physics, University of Cyprus, 1, Panepistimiou Street, 2109 Aglantzia, Cyprus*
[2]*CEICO, Institute of Physics of the Czech Academy of Sciences, Na Slovance 2, 18221 Praha 8 Czech Republic*
[3]*Department of Physics, Brown University, 182 Hope Street, Providence, Rhode Island 02912, USA*

(Received 7 November 2017; published 26 December 2017)

We demonstrate that the Vlasov equation describing collisionless self-gravitating matter may be solved with the so-called Schrödinger method (ScM). With the ScM, one solves the Schrödinger-Poisson system of equations for a complex wave function in d dimensions, rather than the Vlasov equation for a $2d$-dimensional phase space density. The ScM also allows calculating the d-dimensional cumulants directly through quasilocal manipulations of the wave function, avoiding the complexity of $2d$-dimensional phase space. We perform for the first time a quantitative comparison of the ScM and a conventional Vlasov solver in $d = 2$ dimensions. Our numerical tests were carried out using two types of cold cosmological initial conditions: the classic collapse of a sine wave and those of a Gaussian random field as commonly used in cosmological cold dark matter N-body simulations. We compare the first three cumulants, that is, the density, velocity and velocity dispersion, to those obtained by solving the Vlasov equation using the publicly available code `ColDICE`. We find excellent qualitative and quantitative agreement between these codes, demonstrating the feasibility and advantages of the ScM as an alternative to N-body simulations. We discuss, the emergence of effective vorticity in the ScM through the winding number around the points where the wave function vanishes. As an application we evaluate the background pressure induced by the non-linearity of large scale structure formation, thereby estimating the magnitude of cosmological backreaction. We find that it is negligibly small and has time dependence and magnitude compatible with expectations from the effective field theory of large scale structure.

DOI: 10.1103/PhysRevD.96.123532

I. INTRODUCTION

Cold dark matter (CDM) is one of the necessary ingredients of the concordance model of modern cosmology, the ΛCDM model. The CDM model explains the amount of Large-Scale Structure (LSS) in the Universe and the formation of halos where galaxies develop and evolve. According to the ΛCDM model initially small density perturbations evolve into bound structures, for instance CDM halos, that are themselves distributed within the cosmic web composed of superclusters, filaments and sheets [1–3]. The morphology of the cosmic web and the clustering of CDM depends sensitively on the cosmological parameters. Thus, accurate modeling and theoretical understanding of the CDM dynamics is required to infer these parameters from observations.

The microphysical nature of CDM is still unknown and it is generally assumed to be composed of a particle species (or perhaps many) which otherwise remains undetected at the present time. In this article, we are interested in the modeling of the dynamics of self-gravitating collisionless (= dark) matter (DM), that may be used to describe a wide variety of particle candidates. In particular, we are interested in cold DM (CDM), where "cold" from the point of view of LSS formation simply means that a smooth density $n(\boldsymbol{x})$ and velocity $\boldsymbol{u}(\boldsymbol{x})$ field suffice to describe the initial DM matter phase space distribution $f(\boldsymbol{x},\boldsymbol{p})$. In other words, $f(\boldsymbol{x},\boldsymbol{p})$ is nonzero only on a three-dimensional sheet defined by $\boldsymbol{p} = m\boldsymbol{u}(\boldsymbol{x})$, and moreover, $\boldsymbol{u}(\boldsymbol{x})$ is single valued. This situation is usually referred to as the single stream regime of CDM.

If cold initial conditions are used at an initial time when linear perturbation theory still applies, the Poisson equation approximates the Einstein equations on all scales relevant for LSS and halo formation (see for instance [4,5]) justifying the usual use of Newtonian gravity and non-relativistic equations in general. Furthermore, gravitational two-body collisions are suppressed due to the presence of a large number of particles in the systems of interest, so that the phase space dynamics of the 1-particle distribution function is collisionless [6]. Therefore, the time evolution of the phase space density $f(t,\boldsymbol{x},\boldsymbol{p})$ is governed by the Vlasov (the collisionless Boltzmann) equation, also known as Jeans equation [7].

A solution to the Vlasov equation is equivalent to a solution of the coupled infinite hierarchy of equations for the cumulants of the phase space density. In the linear regime of LSS formation, before multistreaming occurs, the

*kopp@fzu.cz
†kyriakos_vattis@brown.edu
‡skordis@fzu.cz

Boltzmann hierarchy of cumulants of the Vlasov equation can be consistently truncated, so that the Vlasov system may be solved by the dust model [1] where the curl part of the velocity and all higher cumulants vanish identically. The dust description breaks down soon after the density contrast evolves into the non-linear regime, as this is generally followed by caustic formation, that is, "shell-crossing" singularities. Consequently, multiple streams occur, vorticity and higher cumulants are generated, and solving the full Vlasov equation is warranted from that point onwards. A popular way of providing approximate solutions to the Vlasov equation, and thus, determining the non-linear evolution of CDM, is through the use of N-body simulations, see for instance [2,8–12].

In most applications, one is not interested in the fine-grained distribution of particles, or the fine details of the distribution function, but rather at the lowest cumulants: density, velocity and velocity dispersion (perhaps even higher cumulants could be of interest). The route to the cumulants via the high-dimensional phase space seems, however, unavoidable if the hierarchy cannot be truncated. Fortunately, this is unnecessary if a different method of solving the Vlasov equation is used, as we describe below in more detail.

The Schrödinger method (ScM), originally proposed in the context of plasma physics in [13] and later independently in the context of gravity by Widrow and Kaiser [14,15], is a numerical technique for approximating solutions to the Vlasov equation while avoiding the difficulties of dealing with phase space. With this method, CDM is modelled as a complex scalar field obeying the coupled Schrödinger-Poisson equations (SPE) [16–18], where $\hbar$ is treated as a free parameter determining the desired phase space resolution. The ScM comprises two steps; (1) solving the SPE with suitably chosen initial conditions and (2) constructing the cumulants of choice. The second step may be performed in two mutually independent ways. Either (2a) by taking the Husimi transform [19] in order to construct a phase space distribution from the wave function and use it to calculate the cumulants. Or, (2b) construct the cumulants directly through quasilocal manipulations of the wave function, avoiding the complexity of $2d$-dimensional phase space. In this work, we follow the second route, that is (2b).

The first three cumulants of a two-dimensional toy cosmological simulation are shown in Fig. 1. From top to bottom, we show the density, the two components of the velocity vector field and the trace of the velocity dispersion tensor. The correspondence between the Vlasov solver `ColDICE` [20] and our implementation of the ScM is depicted by the left and right column. The same initial linear Gaussian random field at $a_{\rm ini} = 1/51$ was used in both cases. The Vlasov solver evolves the two-dimensional phase space sheet in four-dimensional phase space, and we obtained the figures on the left column by subsequent projection of that phase space sheet weighted by suitable

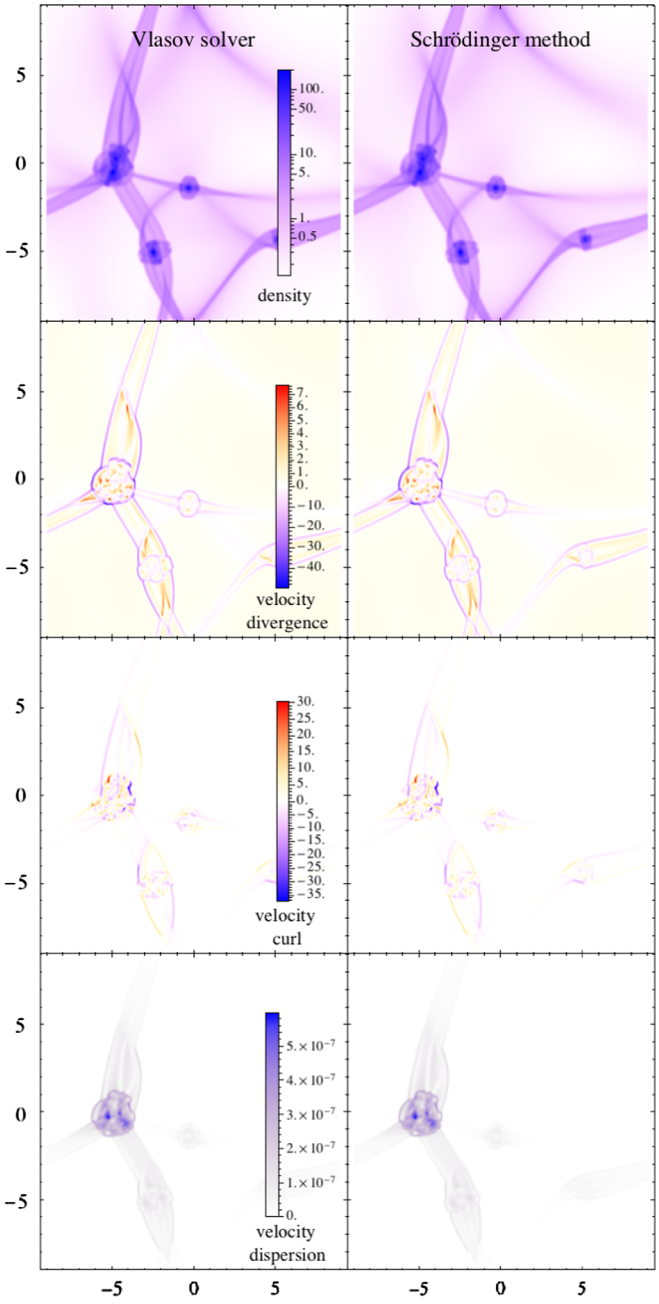

FIG. 1. Time snapshots of a two-dimensional cosmological simulation evolved to the present time $a = 1$. Both codes were started with the same single-stream initial conditions, set up using the Zel'dovich approximation at $a_{\rm ini} = 1/51$. From top to bottom: density, velocity divergence, velocity curl and trace of the velocity dispersion tensor. The left column shows the smoothed results of the two-dimensional version of the Vlasov solver `ColDICE` [20]. The result of the Schrödinger method is shown in the right column. The differences are barely visible by eye. A quantitative comparison is presented in Sec. IV.

powers of $\boldsymbol{u}$ onto the two-dimensional Eulerian space, followed by Gaussian smoothing. The figures on the right column have been obtained by evolving a complex wave function in two-dimensional Eulerian space and

TABLE I. Comparison between the Schrödinger method, and two other continuum formulations of CDM: the dust fluid that ceases to describe CDM after shell-crossing and the Lagrangian formulation of the Vlasov equation with cold initial conditions, that can be seen as the continuum definition of CDM. The mathematical correspondence of $f_{\rm H}$ with cold initial conditions and the coarse-grained CDM phase space density $\bar{f}_{\rm c}$ (18) is established by virtue of (29) and numerically verified in the two-dimensional case in Sec. IV.

	ScM: $f_{\rm H}(t,\boldsymbol{x},\boldsymbol{u})$, Sec. II E	Dust: $f_{\rm d}(t,\boldsymbol{x},\boldsymbol{u})$, Sec. II B	CDM: $f_{\rm c}(t,\boldsymbol{x},\boldsymbol{u})$, Sec. II C
Degrees of freedom (d.o.f.) type	$1\times\mathbb{C}$: $\psi(t,\boldsymbol{x})$	$2\times\mathbb{R}$: $n_{\rm d}(t,\boldsymbol{x}),\phi_{\rm d}(t,\boldsymbol{x})$	$2\times\mathbb{R}^d$: $\boldsymbol{X}(t,\boldsymbol{q}),\boldsymbol{U}(t,\boldsymbol{q})$
Number of d.o.f.	2	2	$2d$
Equations of motion	1st order SPE (21)	1st order fluid equations (10)	1st order trajectories (12)
Singularity-free d.o. fs	✓	✗	✓
$f(\boldsymbol{x},\boldsymbol{u})$ constructed from	$\psi(\boldsymbol{x})$, quasilocal (27)	$n_{\rm d}(\boldsymbol{x}),\boldsymbol{\nabla}\phi_{\rm d}(\boldsymbol{x})$, local (11)	$\boldsymbol{X}(\boldsymbol{q}),\boldsymbol{U}(\boldsymbol{q})$, nonlocal (14)
$M^{(n)}(\boldsymbol{x})$ constructed from	$\partial_x^{0\le m\le n}\psi(\boldsymbol{x})$, quasilocal (34)	$n_{\rm d}(\boldsymbol{x}),\boldsymbol{\nabla}\phi_{\rm d}(\boldsymbol{x})$, local	$\boldsymbol{X}(\boldsymbol{q}),\boldsymbol{U}(\boldsymbol{q})$, nonlocal (15)
Vlasov equation (4) solved	Approximately $(\hbar,\sigma_x)$	Exactly until shell-crossing	Exactly
Multistreaming and virialization	✓	✗	✓
Initial conditions type	Arbitrary, incl. cold (37)	Cold (11)	Cold (13)

subsequently constructing the corresponding coarse-grained cumulants through simple spatial differentiation of the wave function, again followed by spatial coarse graining. Although these methods are vastly different both in implementation and also conceptually, the results are barely distinguishable by eye.

A. Objective

The main result of this article is the extension of all previous one-dimensional tests of the ScM [14,15,21–24],[1] to two-dimensional configurations, using a single smooth wave function on a cosmological background with nearly cold initial conditions, similarly to [23]. In contrast to [23], we also quantitatively show that the resulting first three cumulants—density, velocity and velocity dispersion—are in good correspondence with the same quantities extracted from a conventional state-of-the-art Vlasov code, `ColDICE` [20]. This is highly non-trivial, since as outlined in Table I, the Vlasov equation with cold initial conditions requires $2d$ degrees of freedom (d.o.f.) to encode the phase space sheet, whereas the ScM requires only two, independent of the spatial dimension d. Therefore, while the success of the ScM for $d=1$ might have been a coincidence due to the matching numbers of d.o.f., its success in $d=2$ gives strong evidence that the ScM will work for any dimension d. Furthermore, we extend the work of [23] by considering non-symmetric initial conditions, in particular, a Gaussian random field akin to standard cosmological simulations. This is another important milestone in showing the generality of the ScM as a method for solving the Vlasov equation. In addition, our work outlines an efficient algorithm for determining moments and cumulants from snapshots of the wave function at any desired time.

[1]A method different from ScM where N wave functions are coupled via the Poisson equation, was shown to accurately solve the Vlasov equation in one-dimensional situations in [25] without the necessity of coarse graining, see also [26,27] for a mathematical treatment.

B. Outline

This article is organized as follows. In Sec. II, we review the connection between the gravitational N-body problem, the phase space description in terms of the Vlasov equation and its connection to the dust fluid and Lagrangian formulation of the Vlasov equation. We review the connection between the Husimi distribution and the coarse-grained Vlasov distribution function. Furthermore we review the algorithm to directly construct moments and cumulants that approximately satisfy the Boltzmann hierarchy in a way that circumvents the full phase space and is therefore easy to implement.

In Sec. III, we describe the numerical implementation of our experimental two-dimensional Schrödinger code. In Sec. IV, we investigate cosmological simulations of two different types of initial conditions, a two-dimensional pancake collapse as well as a more realistic Gaussian random field, to provide further empirical proof of the accuracy and feasibility of the ScM. We quantitatively compare cumulants to the corresponding quantities obtained with a state of the art Vlasov code `ColDICE`.

In our discussion section, Sec. V, we explain how vorticity arises in the ScM without the seemingly necessary vortical degrees of freedom, a qualitative new phenomenon in $d=2$ dimensions which goes beyond the previous one-dimensional studies. We also demonstrate the advantage of the ScM, with two applications. First, we evaluate the dynamical pressure induced by the non-linear structure formation—an easy task in the ScM—allowing an estimate of the magnitude of backreaction on the background cosmology. Second, we outline how to calculate the entropy and the free energy. Since the phase space density comes with a fixed coarse-graining scale, the entropy is well defined and will shed new light on the nature of LSS formation.

The reader may also find useful the appendices. In Appendix A, we present Zel'dovich initial conditions.

In Appendix B, we give some further details regarding our numerical implementation. In Appendix C, we describe the one-dimensional continuum formulation of CDM, as it is not readily available in the literature and propose an iterative improvement of the Zel'dovich approximation in the multistream regime. In Appendixes D and E, we collect derivations and proofs, and in Appendix F, we collect various results from [23] in order to assist the reader.

II. MODELING COLD DARK MATTER

The reader already familiar with the ScM or not interested in its details might want to skip this section. For quick reference, the most important equations are highlighted and a summary of the construction algorithm of the phase space density is given at the end of Sec. II E 3, and for moments and cumulants these can be found at the end of Sec. II E 4. It is only the second approach that we explicitly use in this article.

A. N-body to Vlasov

The gravitational N-body problem is defined by the Hamiltonian system

$$E_N = \sum_{i=1}^{N}\left(\frac{\boldsymbol{u}_i^2}{2a^2} - \frac{mG}{2a}\sum_{j=1,j\neq i}^{N}\frac{1}{|\boldsymbol{x}_i-\boldsymbol{x}_j|}\right)$$
$$\dot{\boldsymbol{x}}_i = \frac{\partial E_N}{\partial \boldsymbol{u}_i}, \qquad \dot{\boldsymbol{u}}_i = -\frac{\partial E_N}{\partial \boldsymbol{x}_i} \tag{1}$$

where a is the scale factor, E_N is the energy per particle mass m, $\boldsymbol{x}_i$ is the comoving spatial coordinate of the particle i with associated conjugate momentum $\boldsymbol{p}_i = m\boldsymbol{u}_i$.[2] Defining the exact microscopic, or Klimontovich, phase space density,

$$f_{\mathrm{K}}(t,\boldsymbol{x},\boldsymbol{u}) = \frac{m}{\rho_0}\sum_{i=1}^{N}\delta_{\mathrm{D}}[\boldsymbol{x}-\boldsymbol{x}_i(t)]\delta_{\mathrm{D}}[\boldsymbol{u}-\boldsymbol{u}_i(t)], \tag{2}$$

using the three-dimensional Dirac delta function δ_{D}, the N Hamiltonian equations (1) that determine the phase space trajectories $\{\boldsymbol{x}_i(t),\boldsymbol{u}_i(t)\}$ can be neatly expressed in form of the Klimontovich equation [28]

$$\partial_t f_{\mathrm{K}} = -\frac{\boldsymbol{u}}{a^2}\cdot\boldsymbol{\nabla}_x f_{\mathrm{K}} + \boldsymbol{\nabla}_x\Phi_{\mathrm{K}}\cdot\boldsymbol{\nabla}_u f_{\mathrm{K}} \tag{3a}$$

$$\Delta\Phi_{\mathrm{K}} = \frac{4\pi G\rho_0}{a}\left(\int \mathrm{d}^3u f_{\mathrm{K}} - 1\right), \tag{3b}$$

which has the simple interpretation that f_{K} is conserved along phase space trajectories, $0 = Df_{\mathrm{K}}/dt = (\partial_t f_{\mathrm{K}} + \dot{\boldsymbol{x}}\cdot\boldsymbol{\nabla}_x f_{\mathrm{K}} + \dot{\boldsymbol{u}}\cdot\boldsymbol{\nabla}_u f_{\mathrm{K}})|_{\boldsymbol{x}=\boldsymbol{x}_i,\boldsymbol{u}=\boldsymbol{u}_i}$ for all i.[3] This follows from the fact that for Hamiltonian systems the phase space trajectories never cross.

For convenience we introduced the (constant) comoving matter background density $\rho_0 = mN/V$, such that background, or spatial average value of f_{K} over some large volume $V\to\infty$, is normalized $\langle\int \mathrm{d}^3u f_{\mathrm{K}}\rangle_V = 1$.

Although it is exactly (3) that N-body simulations solve, it is not feasible to use values of N and m that we expect from particle DM candidates. Even if DM were primordial black holes with $m \simeq 15M_\odot$, possibly the largest m encountered for DM in the literature, current cosmological N-body simulations have particle masses that are 8 orders larger than this value and therefore can only approximate the physical N-body problem. The continuum limit $f(\boldsymbol{x},\boldsymbol{u}) = \lim_{N\to\infty} f_{\mathrm{K}}(\boldsymbol{x},\boldsymbol{u})$ or 'pulverization,' where $N\to\infty$ and $m\to 0$ with $\rho_0 = mN/V$ constant, although an idealization, comes closer to modeling collisonless particle DM. The such defined smooth phase space density satisfies the Vlasov equation

$$\partial_t f = -\frac{\boldsymbol{u}}{a^2}\cdot\boldsymbol{\nabla}_x f + \boldsymbol{\nabla}_x\Phi\cdot\boldsymbol{\nabla}_u f \tag{4a}$$

$$\Delta\Phi = \frac{4\pi G\rho_0}{a}\left(\int \mathrm{d}^3u f - 1\right), \tag{4b}$$

that is, the collisionless Boltzmann equation with a long range gravitational force $\boldsymbol{\nabla}_x\Phi$ determined by f itself. The form of Klimontovich and Vlasov equations, (3) and (4), is identical and therefore the Vlasov equation simply states the conservation of the now continuous phase space density along phase space trajectories of the continuum. While (3) is in effect short-hand notation for the Newtonian equations of motion of N particles, (4) is an evolution equation for a smooth phase space distribution.

The Vlasov equation is often taken as the defining equation of purely self-gravitating, and thus collisionless, non-relativistic matter. It also has a straightforward relativistic generalization, see for instance [29] for a detailed treatment. Although the Vlasov equation is a very useful definition for collisionless DM in the context of LSS formation, it is not sufficient when the discreteness matters, as is the case for the internal dynamics of globular clusters where the number N of particles[4] is only a few thousand [6]. In this case, a better continuum approximation to the N-body dynamics (3) starts with a transformation of (3) into the Bogoliubov-Born-Green-Kirkwood-Yvon

[2]For simplicity and without loss of much generality, we assumed that the mass m is the same for all particles. It is therefore convenient to use $\boldsymbol{u}$ instead of $\boldsymbol{p}$ as phase space coordinate because many equations appear less cluttered.

[3]f_{K} remains nonzero (the height of the six-dimensional δ_{D}) along each particle's phase space trajectory and vanishes everywhere else.

[4]For a globular cluster, the particles are stars such that $m \simeq 1M_\odot$.

(BBGKY) hierarchy for the n-particle distribution functions using an appropriate ensemble average without taking the limit $N \to \infty$. A truncation of this hierarchy at lowest order in $1/N$ gives the Vlasov equation, while the one at second order contains a collision term that takes into account some of the discreteness through the 2-particle correlation function [6,30,31]. Note that cosmological N-body simulations suffer from artificial discreteness effects due to the relatively small $\mathrm{N} \ll N_{\mathrm{phys}}$ and therefore may fail to approximate the Vlasov equation as well as the physical N-body problem.

Moments and Cumulants Most applications of f in cosmology involve only its first few ($n = 0, 1, 2$) moments

$$M^{(n)}_{i_1 \ldots i_n}(\boldsymbol{x}) \equiv \int \mathrm{d}^3u \; u_{i_1} \cdots u_{i_n} f(\boldsymbol{x}, \boldsymbol{u}). \tag{5}$$

In order to calculate the nth moment, it is convenient to define the moment generating function,

$$G(\boldsymbol{x}, \boldsymbol{J}) \equiv \int \mathrm{d}^3u e^{i\boldsymbol{u}\cdot\boldsymbol{J}} f(\boldsymbol{x}, \boldsymbol{u}), \tag{6}$$

such that moments and cumulants are given by

$$M^{(n)}_{i_1 \cdots i_n} = (-i)^n \frac{\partial^n G}{\partial J_{i_1} \ldots \partial J_{i_n}}\bigg|_{\boldsymbol{J}=0} \tag{7a}$$

$$C^{(n)}_{i_1 \cdots i_n} \coloneqq (-i)^n \frac{\partial^n \ln G}{\partial J_{i_1} \ldots \partial J_{i_n}}\bigg|_{\boldsymbol{J}=0}. \tag{7b}$$

Taking time derivatives of $C^{(n)}$ or $M^{(n)}$ and using the Vlasov equation (4a) to eliminate $\partial_t f$ at the right-hand side of (7), results in an infinite coupled collection of first order time evolution equations for the $C^{(n)}$ or $M^{(n)}$, the Boltzmann hierachy, see [23] for details. The first 3 moments are

$$M^{(0)} = n, \tag{8a}$$

$$M^{(1)}_i \eqqcolon n u_i \tag{8b}$$

$$M^{(2)}_{ij} \eqqcolon n u_i u_j + n\Sigma_{ij}, \tag{8c}$$

and the resulting cumulants are then determined by them as

$$C^{(0)} = \ln n \tag{8d}$$

$$C^{(1)}_i = u_i \tag{8e}$$

$$C^{(2)}_{ij} = \Sigma_{ij}. \tag{8f}$$

The physical interpretation is as follows. The scalar field $n(t, \boldsymbol{x})$ is the density, the vector field $u_i(t, \boldsymbol{x})$ is the mass-weighted velocity related to the peculiar velocity as $v_i = u_i/a$ and the tensor field $\Sigma_{ij}(t, \boldsymbol{x})$ is the mass-weighted velocity dispersion.

The physical significance of the moments $M^{(1)}$ and $M^{(2)}$ becomes clear when we consider the four-dimensional energy momentum tensor $T_{\mu\nu} = \frac{\rho_0}{\sqrt{-g}} \times \int \frac{du_1 du_2 du_3}{u^0(u_j)} u_\mu u_\nu f(x^\alpha, u_i)$ in the Newtonian limit. Its components with respect to coordinates $x^\alpha = (t, \boldsymbol{x})$ are

$$T_{00} = \rho_0 M^{(0)}/a^3 \tag{9a}$$

$$T_{0i} = -\rho_0 M^{(1)}_i/a^3 \tag{9b}$$

$$T_{ij} = \rho_0 M^{(2)}_{ij}/a^3, \tag{9c}$$

where we have neglected any metric perturbations and relativistic effects, such that $g_{00} = -1$, $g_{0i} = 0$, $g_{ij} = a^2\delta_{ij}$ and $u^0 = 1$.[5]

B. Dust to Vlasov

The dust model is a pressureless perfect fluid with density $n_{\mathrm{d}}(t, \boldsymbol{x})$ and an irrotational velocity $\boldsymbol{u}_{\mathrm{d}}(t, \boldsymbol{x}) = \boldsymbol{\nabla}\phi_{\mathrm{d}}(t, \boldsymbol{x})$[6] satisfying the continuity, Euler and Poisson equations

$$\partial_t n_{\mathrm{d}} = -\frac{1}{a^2}\boldsymbol{\nabla} \cdot (n_{\mathrm{d}}\boldsymbol{u}_{\mathrm{d}}), \tag{10a}$$

$$\partial_t \boldsymbol{u}_{\mathrm{d}} = -\frac{1}{a^2}(\boldsymbol{u}_{\mathrm{d}} \cdot \boldsymbol{\nabla})\boldsymbol{u}_{\mathrm{d}} - \boldsymbol{\nabla}\Phi_{\mathrm{d}}, \tag{10b}$$

$$\boldsymbol{\nabla} \times \boldsymbol{u}_{\mathrm{d}} = 0 \tag{10c}$$

$$\Delta\Phi_{\mathrm{d}} = \frac{4\pi G\rho_0}{a}(n_{\mathrm{d}} - 1). \tag{10d}$$

These equations describe cold collisionless DM (CDM) in the so-called "single stream" regime. It is therefore often used as the defining equation for CDM in many analytical studies of LSS formation. The dust phase space density is given by

$$f_{\mathrm{d}}(t, \boldsymbol{x}, \boldsymbol{u}) = n_{\mathrm{d}}(t, \boldsymbol{x})\delta_{\mathrm{D}}[\boldsymbol{u} - \boldsymbol{\nabla}\phi_{\mathrm{d}}(t, \boldsymbol{x})] \tag{11}$$

and solves the Vlasov equation (4) automatically until the appearance of so-called shell-crossing singularities or caustics where n_{d} diverges.[7] For cold initial conditions,

[5]This is a good approximation in the Newtonian (or Poisson) gauge for non-relativistic matter.

[6]We will drop very often the argument $\boldsymbol{x}$ from the velocity $\boldsymbol{u}(\boldsymbol{x})$ and simply write $\boldsymbol{u}$ whenever it is clear from the context that $\boldsymbol{u}$ is not a coordinate in phase space, but a vector field in real space.

[7]The different types of singularities in the Zel'dovich approximation have been classified in [32].

where f initially has the form (11), these singularities generically occur and are harmless in the Vlasov equation (4) but lead to the break-down of the dust fluid description (10). This is because after shell crossing, f can no longer be expressed as the product (11). The product form of $f_{\rm d}$ makes all the cumulants vanish with $n > 1$. After shell-crossing, however, f generally produces non-zero vorticity invalidating (10c), and non-zero velocity dispersion $C^{(2)}_{ij}$ thus modifying the Euler equation (10b). The equation of motion for $C^{(2)}_{ij}$ contains $C^{(3)}_{ijk}$, and so on, such that a truncation of the Boltzmann hierarchy is no longer possible, see [23,33].

C. CDM to Vlasov

A useful continuum definition of CDM is a phase space density $f_{\rm c}$ that is solution of the Vlasov equation (4) with initial conditions of the form (11).

Although after shell crossing $f_{\rm c}$ cannot be expressed solely as function of $\boldsymbol{x}$, it can still be expressed as function of the Lagrangian coordinate $\boldsymbol{q}$, the continuum generalization of the particle label i. For this we introduce the particle trajectories $\boldsymbol{X}(t,\boldsymbol{q})$ which smoothly depend on the initial positions $\boldsymbol{q}$. The equations of motions for $\boldsymbol{X}(t,\boldsymbol{q})$ and $\boldsymbol{U}(t,\boldsymbol{q})$ are in full analogy to (1) given by

$$\begin{aligned} a^2\dot{\boldsymbol{X}}(\boldsymbol{q}) &= \boldsymbol{U}(\boldsymbol{q}) \\ \dot{\boldsymbol{U}}(\boldsymbol{q}) &= \frac{G\rho_0}{a}\int \mathrm{d}^3q'\,\frac{\boldsymbol{X}(\boldsymbol{q})-\boldsymbol{q}'}{|\boldsymbol{X}(\boldsymbol{q})-\boldsymbol{q}'|^3} - \frac{\boldsymbol{X}(\boldsymbol{q})-\boldsymbol{X}(\boldsymbol{q}')}{|\boldsymbol{X}(\boldsymbol{q})-\boldsymbol{X}(\boldsymbol{q}')|^3}, \end{aligned} \tag{12}$$

where we have assumed that

$$\boldsymbol{X}(\boldsymbol{q}, t\to 0) = \boldsymbol{q}, \tag{13}$$

corresponding to growing mode initial conditions of (10). We explicitly wrote $-\boldsymbol{\nabla}_x\Phi$ in terms of $\boldsymbol{X}(\boldsymbol{q})$ to make it manifest that shell-crossing infinities in the density do not necessarily lead to divergencies in $\boldsymbol{X}$ and $\boldsymbol{U}$. See Appendix D for a derivation. Indeed, these variables remain continuous and sufficiently smooth at shell-crossings such that they can be numerically evolved without problems.

Although a numerical implementation of (12) necessarily discretizes $\boldsymbol{X}(t,\boldsymbol{q})$, the continuum formulation allows to keep track of the phase space sheet, which then in turn i) allows to refine the discretization at any time in a well defined manner and ii) leads to much smoother moments (15b) compared to conventional count-in-cells estimators. This is done in codes like ColDICE [20] or the ones presented in [34–37], but does not occur in conventional N-body simulations. For illustration, we consider the one-dimensional case of (12) in Appendix C.

The CDM phase space density $f_{\rm c}$ is the continuum limit of the Klimontovich phase space density (2). It can be constructed from $\boldsymbol{X}(\boldsymbol{q})$ and $\boldsymbol{U}(\boldsymbol{q})$ as

$$f_{\rm c}(t,\boldsymbol{x},\boldsymbol{u}) = \int \mathrm{d}^3q\,\delta_{\rm D}[\boldsymbol{x}-\boldsymbol{X}(\boldsymbol{q})]\delta_{\rm D}[\boldsymbol{u}-\boldsymbol{U}(\boldsymbol{q})] \tag{14a}$$

$$= \sum_{\substack{\boldsymbol{q}\ \text{with}\\ \boldsymbol{x}=\boldsymbol{X}(t,\boldsymbol{q})}} \frac{\delta_{\rm D}[\boldsymbol{u}-\boldsymbol{U}(\boldsymbol{q})]}{|\det\partial_{q^i}X^j(\boldsymbol{q})|} \tag{14b}$$

and satisfies the Vlasov equation (4). Thus the Vlasov equation for cold initial conditions may be solved with the help of six degrees of freedom $\boldsymbol{X}(\boldsymbol{q})$ and $\boldsymbol{U}(\boldsymbol{q})$ (see Appendix E for a derivation), while in the single stream regime, two degrees of freedom, $n_{\rm d}(\boldsymbol{x})$ and $\phi_{\rm d}(\boldsymbol{x})$, are sufficient.

The moments $M^{\rm c}$ are trivially obtained from (14) as

$$M^{{\rm c}(n)}_{i_1,\ldots,i_n}(\boldsymbol{x}) = \int \mathrm{d}^3q\,\delta_{\rm D}(\boldsymbol{x}-\boldsymbol{X}(\boldsymbol{q}))U_{i_1}(\boldsymbol{q})\ldots U_{i_n}(\boldsymbol{q}) \tag{15a}$$

$$= \sum_{\substack{\boldsymbol{q}\ \text{with}\\ \boldsymbol{x}=\boldsymbol{X}(t,\boldsymbol{q})}} \frac{U_{i_1}(\boldsymbol{q})\ldots U_{i_n}(\boldsymbol{q})}{|\det\partial_{q^i}X^j(\boldsymbol{q})|} \tag{15b}$$

and are, like $f_{\rm c}$, nonlocal in $\boldsymbol{q}$ space. The second equalities in (14) and (15), respectively, follow from the properties of the Dirac δ function, $\delta_{\rm D}$.

These sum over streams[8] have to be performed in Vlasov solvers like ColDICE to obtain $M^{{\rm c}(0)} = n_{\rm c}$ in order to solve the Poisson equation at each time step. From (14b) and (15b), it is clear that if there is only a single stream, such that $\boldsymbol{x} = \boldsymbol{X}(t,\boldsymbol{q})$ is invertible for $\boldsymbol{q}$, the resulting $f_{\rm c}$ is of the product form (11). The assumed initial conditions (13) thus guarantee that there is an early time where $f_{\rm c} = f_{\rm d}$.

It is also worth mentioning that (12) makes it manifest that the acceleration $\dot{\boldsymbol{U}}(\boldsymbol{q})$ of the stream at $\boldsymbol{q}$ is determined by all streams with the same $\boldsymbol{X}(\boldsymbol{q})$. This is not the case in conventional treatments of the Lagrangian formulation of CDM, where the invertibility of $\partial_{q^i}X^j(\boldsymbol{q})$ is assumed and used in reformulating (12) into an equation local in $\boldsymbol{q}$. Solutions of this transformed equation lead necessarily to unphysical behavior after shell-crossing [39]. We discuss this further in App. C.

[8]Due to the assumed initial conditions (13), the map $\boldsymbol{X}(t,\boldsymbol{q})$ belongs to the homotopy class of the identity, whose degree is one. The degree of a function $\boldsymbol{X}(\boldsymbol{q})$ at a regular point $\boldsymbol{x}$ is the natural number of points $\boldsymbol{q}$ for which $\boldsymbol{x} = \boldsymbol{X}(\boldsymbol{q})$. In our case, this is the number of streams. A point $\boldsymbol{x}$ is regular if it does not lie on a shell-crossing caustic. Now, according to a theorem of differential topology, see § 4 of [38], the parity of the degree is independent of the regular point $\boldsymbol{x}$ and also independent of the representative $\boldsymbol{X}(\boldsymbol{q})$ of the homotopy class. Therefore, the number of streams is always finite and odd, excluding the zero-measure subset of $\boldsymbol{x}$ on caustics.

D. Coarse-grained Vlasov

1. General case

The coarse-grained phase space density

$$\bar{f}(t,\boldsymbol{x},\boldsymbol{u}) = \int \frac{\mathrm{d}^3x'\mathrm{d}^3u'}{(2\pi\sigma_x\sigma_u)^3} e^{-\frac{(\boldsymbol{x}-\boldsymbol{x}')^2}{2\sigma_x{}^2}-\frac{(\boldsymbol{u}-\boldsymbol{u}')^2}{2\sigma_u{}^2}} f(t,\boldsymbol{x}',\boldsymbol{u}'),$$
$$= e^{\frac{\sigma_x{}^2}{2}\Delta_x+\frac{\sigma_u{}^2}{2}\Delta_u}\{f\} \tag{16}$$

is obtained from f through convolution with a Gaussian filter with width σ_x and σ_u in $\boldsymbol{x}$ and $\boldsymbol{u}$ space. For notational simplicity we will use a shorthand operator representation of the Gaussian smoothing defined in the second line of (16). The corresponding coarse-grained Vlasov equation can be obtained by applying the smoothing operator on (4), see [23,40].

The moments $\bar{M}^{(n)}$ of $\bar{f}$ are simply obtained from the moments of f as

$$\bar{M}^{(0)} = e^{\frac{\sigma_x{}^2}{2}\Delta_x}\{M^{(0)}\} \tag{17a}$$

$$\bar{M}^{(1)}_i = e^{\frac{\sigma_x{}^2}{2}\Delta_x}\{M^{(1)}_i\} \tag{17b}$$

$$\bar{M}^{(2)}_{ij} = e^{\frac{\sigma_x{}^2}{2}\Delta_x}\{M^{(2)}_{ij}\} + \sigma_u{}^2\bar{M}^{(0)}\delta_{ij}. \tag{17c}$$

The cumulants $\bar{C}^{(n)}$ are obtained from the $\bar{M}^{(n)}$ in the standard fashion according to (8) with all quantities barred. Note that in particular $\bar{u}_i \neq e^{\frac{\sigma_x{}^2}{2}\Delta_x}\{u_i\}$, and instead $\bar{u}_i = \bar{M}^{(1)}_i/\bar{n}$. The second term in (17c) arises through the spreading of the velocity distribution by the Gaussian with variance σ_u. Note that the first two moments are not affected by σ_u.

The coarse-grained phase space density $\bar{f}$ has many desirable features that f does not have. For instance $\bar{f}$ is no longer exactly conserved along phase space trajectories which allows us to properly define phase mixing, virialization and entropy production [40,41]. This also makes $\bar{f}$ better behaved from a numerical point of view since $\bar{f}$ cannot develop structures below the scales σ_x and σ_u, in contrast to f which continues to develop ever smaller structures over time.

Thus a method allowing direct computation of $\bar{f}$ without first computing f is of practical interest. Since $\bar{f}$ can be approximated by coarse graining f_{K} directly without taking the limit that brought us to the Vlasov equation (4), a straightforward method to produce an approximation to $\bar{f}$ is to run a N-body simulation [2,8–12,20,37] and sample the phase space density using the particles.[9]

[9]The actually achieved resolution $\sigma_x\sigma_u$ is hard to estimate since it strongly depends on the method and usually is not constant in space and time.

2. CDM

The coarse-grained continuum limit of CDM (14) is obtained by inserting (14a) into (16)

$$\bar{f}_{\mathrm{c}}(t,\boldsymbol{x},\boldsymbol{u}) = \frac{1}{(2\pi)^3\sigma_x{}^3\sigma_u{}^3}\int \mathrm{d}^3q e^{-\frac{[\boldsymbol{x}-\boldsymbol{X}(t,\boldsymbol{q})]^2}{2\sigma_x{}^2}} e^{-\frac{[\boldsymbol{u}-\boldsymbol{U}(t,\boldsymbol{q})]^2}{2\sigma_u{}^2}}. \tag{18}$$

Similarly, inserting (15a) into (17) shows that the coarse-grained CDM moments

$$\bar{M}^{\mathrm{c}(0)} = \frac{1}{(2\pi)^{3/2}\sigma_x{}^3}\int \mathrm{d}^3q e^{-\frac{[\boldsymbol{x}-\boldsymbol{X}(t,\boldsymbol{q})]^2}{2\sigma_x{}^2}} \tag{19a}$$

$$\bar{M}^{\mathrm{c}(1)}_i = \frac{1}{(2\pi)^{3/2}\sigma_x{}^3}\int \mathrm{d}^3q e^{-\frac{[\boldsymbol{x}-\boldsymbol{X}(t,\boldsymbol{q})]^2}{2\sigma_x{}^2}} U_i(t,\boldsymbol{q}) \tag{19b}$$

$$\bar{M}^{\mathrm{c}(2)}_{ij} = \frac{1}{(2\pi)^{3/2}\sigma_x{}^3}\int \mathrm{d}^3q e^{-\frac{[\boldsymbol{x}-\boldsymbol{X}(t,\boldsymbol{q})]^2}{2\sigma_x{}^2}} U_i(t,\boldsymbol{q})U_j(t,\boldsymbol{q})$$
$$+ \sigma_u{}^2\bar{M}^{\mathrm{c}(0)}\delta_{ij}, \tag{19c}$$

involve $\boldsymbol{X}(\boldsymbol{q})$ and $\boldsymbol{U}(\boldsymbol{q})$, just like $\bar{f}_{\mathrm{c}}$, only in a three-dimensional integral over Lagrangian space. Alternatively one might chose not to simplify (16) and (17) and perform the smoothing only after the sum over streams in (14b) and (15b) has been calculated. It is the second method that we will use in Sec. IV.

E. The Schrödinger method

The Schrödinger method is an alternative way to approximate $\bar{f}$. In the ScM, one constructs a phase space distribution $f_{\mathrm{H}}(t,\boldsymbol{x},\boldsymbol{u})$ at a given time from a smooth complex field $\psi(t,\boldsymbol{x})$ that satisfies the Schrödinger-Poisson equation. The function $f_{\mathrm{H}}(t,\boldsymbol{x},\boldsymbol{u})$ is called the Husimi distribution and is the absolute square of the Husimi-representation of the wave function ψ. The transformation $\psi \to f_{\mathrm{H}}$ is local in time, but involves one quasilocal integral over Eulerian space. Thus, to evaluate $f_{\mathrm{H}}(t,\boldsymbol{x},\boldsymbol{u})$ at points $\boldsymbol{x},\boldsymbol{u}$ one only has to consider a single time snapshot of $\psi(t,\boldsymbol{x}')$ and only points $\boldsymbol{x}'$ in a small neighborhood around $\boldsymbol{x}$.

The phase space resolution of f_{H} is constant in phase space and time. In some applications of simulations of LSS formation, for instance, the investigation of voids or ray-tracing, a spatially and temporally fixed resolution might be desirable.

The ScM offers a compact way to store the entire six-dimensional phase space information in $f_{\mathrm{H}}(\boldsymbol{x},\boldsymbol{u})$ in two, three-dimensional degrees of freedom contained in $\psi(\boldsymbol{x})$. Although the phase space density f_{H} can be easily constructed from ψ, the most useful feature of the ScM is that all moments and cumulants of the phase space distribution, like the density, velocity and velocity dispersion as well as the stress-energy-momentum tensor, can be constructed directly from ψ and its spatial

derivatives without the need to first construct the phase space density and subsequent cumbersome projections in velocity space. Constructing moments and cumulants involves only taking spatial derivatives of ψ and using a Gaussian filter, which is very efficient to calculate since both processes are quasilocal in space.

This should be contrasted with the case of CDM, where the dynamics of $f(t,\boldsymbol{x},\boldsymbol{u})$ can be compressed into two three-dimensional vector field $\boldsymbol{X}(t,\boldsymbol{q})$, $\boldsymbol{U}(t,\boldsymbol{q})$ satisfying first order differential equations. Therefore one needs to take care of 6 degrees of freedom rather than 2. Similar to $\psi(t,\boldsymbol{x})$ the phase space density $f_{\rm c}$ and moments $M_{\rm c}$ can be directly constructed from $\boldsymbol{X}(t,\boldsymbol{q})$ by a single spatial integration. The integration is, however, nonlocal, whereas the construction of $f_{\rm H}$ and $M_{\rm H}$ is quasilocal. Lastly while the reduction of degrees of freedom from $f(t,\boldsymbol{x},\boldsymbol{u})$ to $\boldsymbol{X}(t,\boldsymbol{q})$ and $\boldsymbol{U}(t,\boldsymbol{q})$ only works for dust initial conditions (11), the ScM works for general initial $f(t_{\rm ini},\boldsymbol{x},\boldsymbol{u})$.

1. The Schrödinger-Poisson equation

The nonrelativistic Schrödinger-Poisson equation (SPE) in a ΛCDM universe with scale factor a can be derived from the following action

$$A[\bar{\psi},\psi] = m\int \mathrm{d}t\mathrm{d}^3x\left(i\tilde{\hbar}\,\bar{\psi}(t,\boldsymbol{x})\partial_t\psi(t,\boldsymbol{x}) - \mathcal{E}[\psi]\right) \tag{20a}$$

$$\mathcal{E}[t,\psi,\bar{\psi}] = \frac{\tilde{\hbar}^2}{2a^2}|\boldsymbol{\nabla}_x\psi(t,\boldsymbol{x})|^2 - \frac{\rho_0 G}{2a}\int \mathrm{d}^3x'\,\frac{|\psi(t,\boldsymbol{x})|^2|\psi(t,\boldsymbol{x}')|^2}{|\boldsymbol{x}-\boldsymbol{x}'|} \tag{20b}$$

upon variation with respect to $\bar{\psi}$ and is given by

$$i\tilde{\hbar}\partial_t\psi = -\frac{\tilde{\hbar}^2}{2a^2}\Delta\psi + \Phi_\psi\psi \tag{21a}$$

$$\Delta\Phi_\psi = \frac{4\pi G\rho_0}{a}(|\psi|^2 - 1), \tag{21b}$$

see for instance [14,23,42]. We have defined

$$\tilde{\hbar} \equiv \frac{\hbar}{m} \tag{22}$$

which simplifies the SPE and can be interpreted as the phase space resolution in coordinates $\boldsymbol{x}$ and $\boldsymbol{u}$. The SPE can also be derived by observing that from the action (20a) it follows that

$$E = \int \mathrm{d}^3x\,\mathcal{E}[t,\psi,i\tilde{\hbar}\,\bar{\psi}] \tag{23a}$$

is the Hamiltonian and $i\hbar\bar{\psi}$ is the canonically conjugate momentum of ψ. Following the rules of Hamiltonian mechanics the SPE is obtained as

$$\frac{d}{dt}\psi = \{E,\psi\} \tag{23b}$$

where $\{\ldots,\ldots\}$ is the Poisson bracket.[10] This shows the close analogy to the Hamiltonian system (1) of N-particles[11] and is of practical use since E will be employed later to test the accuracy of the numerical solution of the SPE (21).

The extra -1 in the Poisson equation (21b) implements the cosmological boundary conditions and may be derived if one starts with the action of general relativity and a real Klein-Gordon field upon taking the nonrelativistic and small-scale limit in the conformal Newtonian gauge, see [43].[12]

2. Madelung representation: relation to the dust fluid

Using the so-called Madelung representation for the wave function

$$\psi(\boldsymbol{x}) =: \sqrt{n_\psi(\boldsymbol{x})}\exp\left(i\phi(\boldsymbol{x})/\tilde{\hbar}\right) \tag{24}$$

with n_ψ and ϕ real, and $n_\psi \neq 0$ the SPE (21) can be transformed into a set of fluidlike equations upon defining $\boldsymbol{u}_\psi \equiv \boldsymbol{\nabla}\phi$, the Madelung-Poisson equation [44]

$$\partial_t n_\psi = -\frac{1}{a^2}\boldsymbol{\nabla}_x\cdot(n_\psi\boldsymbol{u}_\psi) \tag{25a}$$

$$\partial_t\boldsymbol{u}_\psi = -\frac{1}{a^2}(\boldsymbol{u}_\psi\cdot\boldsymbol{\nabla})\boldsymbol{u}_\psi - \boldsymbol{\nabla}\Phi_\psi + \frac{\tilde{\hbar}^2}{2a^2}\boldsymbol{\nabla}\left(\frac{\Delta\sqrt{n_\psi}}{\sqrt{n_\psi}}\right) \tag{25b}$$

$$\boldsymbol{\nabla}\times\boldsymbol{u}_\psi = 0 \tag{25c}$$

$$\Delta\Phi_\psi = \frac{4\pi G\rho_0}{a}(n_\psi - 1). \tag{25d}$$

Comparing them to the dust equations (10) it becomes transparent that the only difference is the single extra term in the Euler equation proportional to $\tilde{\hbar}^2$, the so-called "quantum pressure,"

$$Q \equiv -\frac{\tilde{\hbar}^2}{2a^2}\frac{\Delta\sqrt{n_\psi}}{\sqrt{n_\psi}}. \tag{26}$$

[10] $\{A,B\} \equiv \int \mathrm{d}^3x\,\frac{\delta A}{\delta[i\tilde{\hbar}\,\bar{\psi}(\boldsymbol{x})]}\frac{\delta B}{\delta\psi(\boldsymbol{x})} - \frac{\delta B}{\delta[i\tilde{\hbar}\,\bar{\psi}(\boldsymbol{x})]}\frac{\delta A}{\delta\psi(\boldsymbol{x})}$. The time evolution of a general $A = A[t,\psi]$ is then given as $dA/dt = \partial_t A + \{E,A\}$. For $A = \psi(\boldsymbol{x}')$ and the rules of functional derivatives one recovers (23b).

[11] Since $\mathcal{E}(\psi,\bar{\psi}) = \mathcal{E}(\bar{\psi},\psi)$ the second Hamiltonian equation for the canonical momentum $i\hbar\bar{\psi}$ is just the complex conjugate of the SPE (23b), see [42].

[12] Note that our normalization of ψ is different from [43]. We chose $\langle|\psi|^2\rangle_V = 1$ for convenience rather than the more natural $\langle|\psi|^2\rangle_V = \rho_0 a^{-3}$.

Thus, if ∇Q is small compared to the other terms in (25b), one can maintain $n_\psi = n_{\rm d}$ and $\phi = \phi_{\rm d}$ to arbitrary precision during time evolution choosing $\tilde{\hbar}$ sufficiently small.

The dynamics of the Madelung-Poisson equation is such that sooner or later, barring fine-tuned initial conditions, Q will become important, independent of the chosen $\tilde{\hbar}$. It turns out that for initial conditions where the quantum pressure can be neglected, the locations in time and space where Q becomes large are close to those where shell crossing happens in the dust fluid. Indeed, if Q becomes large it signals the impending breakdown of the Madelung-Poisson equation (25): for initial conditions that make Q small, $\boldsymbol{u}_\psi$ diverges at nearly the same locations in space and time where $n_{\rm d}$ of the dust model diverges. It turns out that $\boldsymbol{u}_\psi = \infty$ events are accompanied by $n_\psi = 0$ and thus a vanishing ψ.

This seemingly contrived situation poses no problems in the SPE (21) which can be numerically evolved through these events without any pathologies if one choses to split ψ into real and imaginary parts, $\Re(\psi)$ and $\Im(\psi)$, rather than amplitude and phase. The phase is ill-defined when $\psi = 0$ and the Madelung equations (25) no longer follow from (21) if $n_\psi = 0$.[13] In Fig. 2, we show part of a simulation snapshot of the same simulation shown in Fig. 1 but at an earlier time. While our dynamical variables $\Re(\psi)$ and $\Im(\psi)$, shown in the upper panel, are perfectly smooth, the phase $\phi/\tilde{\hbar}$ of ψ, shown in the lower right panel, has several pointlike singularities which persist in time and which coincide with locations where $n_\psi = 0$. The phase has a nonzero winding number around these singularities, observed by following the color gradient around them. This circulation is the analogue of microscopic vorticity in the ScM and is discussed in more detail in Sec. V A.

We now present the definition of the ScM, that is, a procedure to extract approximate solutions to the Vlasov equation (4) from solutions of the SPE for the most general case where f is allowed to exhibit shell-crossing and mutlistreaming.

[13]It is known that Madelung and Schrödinger equations are not necessarily equivalent [45], see also the discussion of Sec. II A in [22]. We therefore recommend, in contrast to a comment in [46], not to use the Madelung equations as a replacement for the Schrödinger equation, since the Madelung equations might not give all solutions, or even give wrong solutions [45]. The reason is that even if the singularities [22,23] are dealt with, for instance, by using the momentum current $\boldsymbol{j}_\psi = n_\psi \boldsymbol{u}_\psi$ as the dynamical variable rather than the velocity $\boldsymbol{u}_\psi$, one still has to implement the constraint (58) that ensures that $\boldsymbol{u}_\psi$ is the gradient of a phase, or in other words that resulting ψ is a single valued complex function. We thus expect that the applicability of a code based on the Madelung equations, like [47], is limited to situations where nodes do not develop, and therefore is applicable only when the analogue of shell-crossing does not occur in the wave function. See Chapter 15.3 of [48] for an introduction to problems and possible solutions when one choses to stay close to the Madelung equations.

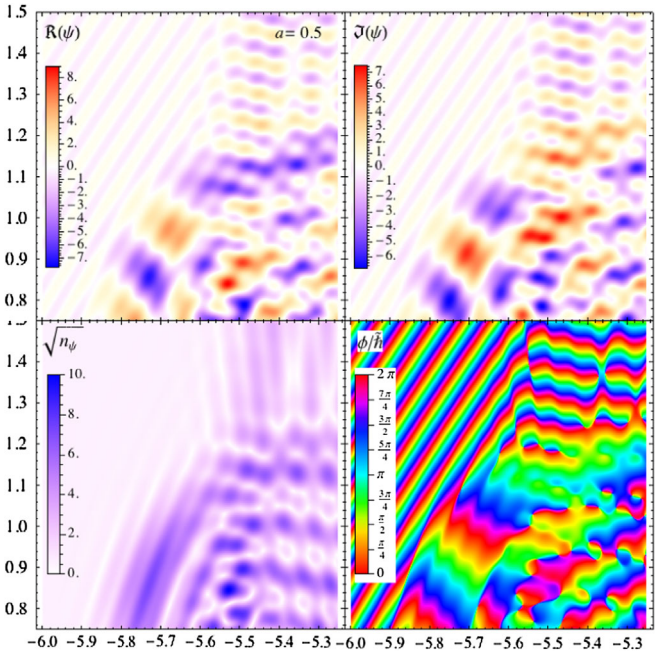

FIG. 2. A small region of width 0.75 Mpc (309 pixels) from a 20 Mpc (8192 pixels) wide simulation box (the units on the axis are in Mpc). The wave function ψ has been evolved from linear Gaussian random field initial conditions with $n_\psi = n_{\rm d}$ and $\phi = \phi_{\rm d}$ into the deeply nonlinear regime, see Sec. IV B for details. The top two panels show the dynamical variables $\Re(\psi)$ and $\Im(\psi)$, whereas the panels on the bottom show amplitude $\sqrt{n_\psi}$ and phase $\phi/\tilde{\hbar}$ of ψ.

3. The Husimi distribution: relation to the Vlasov equation

The so-called Husimi-representation $\psi_{\rm H}(\boldsymbol{x},\boldsymbol{u})$ of the wave function $\psi(\boldsymbol{x})$ in terms of Gaussian wave packets gives rise to the (manifestly non-negative) Husimi phase space distribution [19][14]

$$f_{\rm H}(t,\boldsymbol{x},\boldsymbol{u}) := |\psi_{\rm H}(t,\boldsymbol{x},\boldsymbol{u})|^2 \tag{27a}$$

$$\psi_{\rm H}(t,\boldsymbol{x},\boldsymbol{u}) := \int {\rm d}^d x'\, K_{\rm H}(\boldsymbol{x},\boldsymbol{x}',\boldsymbol{u})\psi(t,\boldsymbol{x}') \tag{27b}$$

$$K_{\rm H}(\boldsymbol{x},\boldsymbol{x}',\boldsymbol{u}) := \frac{\exp\left[-\frac{(\boldsymbol{x}-\boldsymbol{x}')^2}{4{\sigma_x}^2} - \frac{i}{\tilde{\hbar}}\boldsymbol{u}\cdot\boldsymbol{x}'\right]}{(2\pi\tilde{\hbar})^{d/2}(2\pi{\sigma_x}^2)^{d/4}}. \tag{27c}$$

The spatial coarse graining scale σ_x is the second parameter of the ScM. Together with $\tilde{\hbar}$, it determines the resolution

[14]The function $f_{\rm H}$ calculated this way is manifestly non-negative. It may, however, be also obtained from the Wigner quasiprobability distribution $f_{\rm W}[\psi]$ by applying a Gaussian filter with width σ_x and $\sigma_u = \tilde{\hbar}/(2\sigma_x)$ such that $f_{\rm H} = e^{\frac{\sigma_x^2}{2}\Delta_x + \frac{\sigma_u^2}{2}\Delta_u}\{f_{\rm W}[\psi]\}$. This second route to $f_{\rm H}$ is, however, numerically inconvenient compared to (27), see [23].

$$\sigma_x, \qquad \sigma_u \equiv \frac{\tilde{\hbar}}{2\sigma_x} \tag{28}$$

of the phase space density $f_{\rm H}$ in $\boldsymbol{x}$ and $\boldsymbol{u}$ direction. It can be shown that $f_{\rm H}$ approximates $\bar{f}$ in the sense that

$$\partial_t(f_{\rm H} - \bar{f}) \simeq -\frac{\tilde{\hbar}^2}{24}(\partial_{x_i}\partial_{x_j}\partial_{x_k}\Phi_{\rm H})(\partial_{u_i}\partial_{u_j}\partial_{u_k}f_{\rm H}), \tag{29}$$

where $\Phi_{\rm H} \equiv e^{\frac{\sigma_x^2}{2}\Delta}\{\Phi_\psi\}$, with Φ_ψ from (21b), see [14,21,23] and App. F. Defining

$$S_{\rm V} \equiv -\frac{\boldsymbol{u}}{a^2}\cdot\boldsymbol{\nabla}_x f_{\rm H} + \boldsymbol{\nabla}_x\Phi_{\rm H}\cdot\boldsymbol{\nabla}_u f_{\rm H} \tag{30a}$$

$$S_{\rm cgV} \equiv -\frac{{\sigma_u}^2}{a^2}\boldsymbol{\nabla}_x\cdot\boldsymbol{\nabla}_u f_{\rm H} + {\sigma_x}^2(\partial_{x_i}\partial_{x_j}\Phi_{\rm H})(\partial_{x_i}\partial_{u_j}f_{\rm H}), \tag{30b}$$

$$S_{\tilde{\hbar}} \equiv -\frac{\tilde{\hbar}^2}{24}(\partial_{x_i}\partial_{x_j}\partial_{x_k}\Phi_{\rm H})(\partial_{u_i}\partial_{u_j}\partial_{u_k}f_{\rm H}) \tag{30c}$$

we generally have that $f_{\rm H}$ satisfies the Husimi equation

$$\partial_t f_{\rm H} = S_{\rm V} + S_{\rm cgV} + S_{\tilde{\hbar}} + \mathcal{O}(\tilde{\hbar}^2{\sigma_x}^2, \tilde{\hbar}^4), \tag{31}$$

but requiring that $f_{\rm H}$ also solves the coarse-grained Vlasov equation leads to $\partial_t f_{\rm H} = S_{\rm V} + S_{\rm cgV}$, or even more optimally the Vlasov equation $\partial_t f_{\rm H} = S_{\rm V}$. Thus we know (i) that we can achieve $f_{\rm H} \simeq \bar{f}$ only if quantum corrections to the Vlasov equation are smaller than coarse graining effects

$$|S_{\tilde{\hbar}}| \ll |S_{\rm cgV}|, \tag{32a}$$

and (ii) that $f_{\rm H} \simeq f$, is possible if in addition to condition (32a) the phase space smoothing scales σ_x and σ_u are much smaller than the smallest features of $f_{\rm H}$, or more precisely

$$|S_{\rm cgV}| \ll |S_{\rm V}|. \tag{32b}$$

We present a derivation in App. F.

In practice, we are more concerned with achieving $f_{\rm H} \simeq \bar{f}$, or (32a) since it is anyway practically impossible to determine f with sufficient spatial resolution for an arbitrary long time due to phase mixing. Regions where phase mixing occurs become increasingly better approximated over time by a coarse-grained distribution [41]. Thus having $f_{\rm H}$ merely agree with $\bar{f}$ rather than f is not only acceptable given the finiteness of computational resources, but also from a physical point of view.

On small scales quantum effects can become important as has been demonstrated and discussed in [46,49–51]. In those studies, it was assumed that dark matter is an axionlike particle in a Bose-Einstein condensate and that in the Newtonian limit this situation can be described by the SPE and ψ more accurately than with the Vlasov equation. Independent of the physical interpretation of ψ, it was shown in [49–51] that in halo centers, $|\psi|^2$ has a solitonic profile that transitions around the solitonic core radius r_c into the Navarro-Frenk-White (NFW) profile. Thus outside of r_c, the wave function behaves like collisionless matter and we expect $f_{\rm H} \simeq \bar{f}_c$ which is consistent with the NFW profile, while inside the solitonic radius we would expect $|S_{\tilde{\hbar}}| \simeq |S_{\rm V}|$ such that $f_{\rm H} \neq \bar{f}_c$. Since the soliton core size r_c scales as $r_c \propto \tilde{\hbar}$, see [50], the breakdown of the ScM is under control.

Before we close the section on the Husimi distribution, we want to point out the important difference between the relation of $f_{\rm H}$ to $\bar{f}$ compared to the previously discussed relation between n_d, $\phi_{\rm d}$ and n_ψ, ϕ in Sec. II E 2: the left-hand side of (32) can be kept small even well after the first shell crossing, deep in the multistream regime [14,21,23] by choosing a sufficiently small $\tilde{\hbar}$ and sufficiently large σ_x. In contrast, the quantum pressure Q in (25b) automatically becomes large once the density contrast $n_\psi - 1$ becomes nonlinear and hence the mapping between $n_{\rm d}$, $\phi_{\rm d}$ and n_ψ, ϕ breaks down shortly before shell-crossing. A large Q does not invalidate (32).

Summary for constructing the phase space density: The ScM approximates solutions $f(t,\boldsymbol{x},\boldsymbol{u})$ to the Vlasov equation (4) by constructing the Husimi distribution $f_{\rm H}(t,\boldsymbol{x},\boldsymbol{u})$ at a given time t via (27), which involves a spatial integral of the snapshot of a wave function $\psi(t,\boldsymbol{x})$ that satisfies the SPE (21). Due to the form of $K_{\rm H}$ the $\boldsymbol{x}'$ integration is quasilocal and it is sufficient to use as integration domain a ball centered around $\boldsymbol{x}$ with a radius of a few σ_x. The accuracy of the ScM is controlled by the two parameters $\tilde{\hbar}$ and σ_x via (32).

4. Moments and cumulants

The extraordinary feature of the ScM is that it allows to analytically evaluate the velocity space integral in (6)

$$\begin{aligned} G_{\rm H}(\boldsymbol{x},\boldsymbol{J}) &= \int {\rm d}^d u\, e^{i\boldsymbol{u}\cdot\boldsymbol{J}} f_{\rm H} \\ &= e^{-\frac{1}{2}{\sigma_u}^2\boldsymbol{J}^2} e^{\frac{\sigma_x^2}{2}\Delta}\{G_{\rm W}(\boldsymbol{x},\boldsymbol{J})\} \\ G_{\rm W}(\boldsymbol{x},\boldsymbol{J}) &= \psi\left(\boldsymbol{x}+\frac{\tilde{\hbar}}{2}\boldsymbol{J}\right)\bar{\psi}\left(\boldsymbol{x}-\frac{\tilde{\hbar}}{2}\boldsymbol{J}\right), \end{aligned} \tag{33}$$

and that this expression is quasilocal in space and, therefore, the resulting moments are efficiently evaluated numerically. This has to be contrasted to CDM [see (14b) and (15b)], where the moment generating function is nonlocal in $\boldsymbol{q}$ space or involves a sum over streams.

Using (7a), the first three moments of the Husimi distribution are easily obtained by first evaluating the Wigner moments $M^{{\rm W}(n\leq 2)}$ obtained from $G_{\rm W}$

$$M^{{\rm W}(0)} = |\psi|^2, \tag{34a}$$

$$M_i^{\mathrm{W}(1)} = \tilde{\hbar}\Im\{\psi_{,i}\bar{\psi}\} \tag{34b}$$

$$M_{ij}^{\mathrm{W}(2)} = \frac{\tilde{\hbar}^2}{2}\Re\{\psi_{,i}\bar{\psi}_{,j} - \psi_{,ij}\bar{\psi}\} \tag{34c}$$

and subsequent coarse graining

$$M^{\mathrm{H}(0)} = e^{\frac{{\sigma_x}^2}{2}\Delta}\{M^{\mathrm{W}(0)}\}, =: n^{\mathrm{H}} \tag{34d}$$

$$M_i^{\mathrm{H}(1)} = e^{\frac{{\sigma_x}^2}{2}\Delta}\{M_i^{\mathrm{W}(1)}\} =: n^{\mathrm{H}}u_i^{\mathrm{H}} \tag{34e}$$

$$M_{ij}^{\mathrm{H}(2)} = e^{\frac{{\sigma_x}^2}{2}\Delta}\{M_{ij}^{\mathrm{W}(2)}\} + {\sigma_u}^2 M^{\mathrm{H}(0)}\delta_{ij} =: n^{\mathrm{H}}u_i^{\mathrm{H}}u_j^{\mathrm{H}} + n^{\mathrm{H}}\Sigma_{ij}^{\mathrm{H}}, \tag{34f}$$

where $\Re$ and $\Im$ denote real and imaginary part. Comparing (34f) and (17c) we recognize the same structure and therefore it is the first term of (34f) that should be compared to $e^{\frac{{\sigma_x}^2}{2}\Delta}\{M_{ij}^{(2)}\}$. All higher moments can be similarly calculated from (7a). They are always bilinear in the wave function and its spatial derivatives with an overall spatial Gaussian smoothing. This makes it very easy to evaluate $M_{\mathrm{H}}^{(n)}(\boldsymbol{x})$ numerically from a time snapshot of $\psi(\boldsymbol{x})$.

The n-th cumulant $C_{\mathrm{H}}^{(n)}(\boldsymbol{x})$ of the Husimi distribution can be constructed from the first n moments according to (7b)

$$C^{\mathrm{H}(0)} = \ln n^{\mathrm{H}} \tag{34g}$$

$$C_i^{\mathrm{H}(1)} = u_i^{\mathrm{H}} = M_i^{\mathrm{H}(1)}/n^{\mathrm{H}} \tag{34h}$$

$$C_{ij}^{\mathrm{H}(2)} = \Sigma_{ij}^{\mathrm{H}} = M_{ij}^{\mathrm{H}(2)}/n^{\mathrm{H}} - u_i^{\mathrm{H}}u_j^{\mathrm{H}}. \tag{34i}$$

All higher cumulants can be constructed in a similar fashion. If ones chooses to work directly with the moments and cumulants without constructing f_{H} then one cannot test the accuracy of the ScM using (32). We can however calculate the moments of the expressions (30) entering the Husimi equation. The first nonvanishing moment of $S_{\tilde{\hbar}}$ is given by $\int \mathrm{d}^3 u u_i u_j u_k S_{\tilde{\hbar}}$, such that we consider

$$S_{\mathrm{V}\,ijk}^{(3)} = -\frac{1}{a^2}\nabla_m M_{ijkm}^{\mathrm{H}(4)} - \nabla_{(i}\Phi_{\mathrm{H}} \cdot M_{jk)}^{\mathrm{H}(2)} \tag{35a}$$

$$S_{\mathrm{cgV}\,ijk}^{(3)} = \frac{{\sigma_u}^2}{a^2}\nabla_{(i}M_{jk)}^{\mathrm{H}(2)} - {\sigma_x}^2\nabla_m\nabla_{(i}\Phi_{\mathrm{H}}\nabla_m M_{jk)}^{\mathrm{H}(2)} \tag{35b}$$

$$S_{\tilde{\hbar}\,ijk}^{(3)} = \frac{\tilde{\hbar}^2}{4}n_{\mathrm{H}}\nabla_i\nabla_j\nabla_k\Phi_{\mathrm{H}}, \tag{35c}$$

where $A_{(ijk)} = A_{ijk} + A_{jki} + A_{kij}$. The minimal requirement to satisfy the ScM condition (32a) thus is

$$|S_{\tilde{\hbar}\,ijk}^{(3)}| \ll |S_{\mathrm{cgV}\,ijk}^{(3)}|, \tag{36a}$$

and similarly, a requirement for (32b) is

$$|S_{\mathrm{cgV}\,ijk}^{(3)}| \ll |S_{\mathrm{V}\,ijk}^{(3)}|. \tag{36b}$$

Summary for constructing the moments and cumulants The ScM allows the construction of moments $M^{\mathrm{H}(n)}(t,\boldsymbol{x})$ and cumulants $C^{\mathrm{H}(n)}(t,\boldsymbol{x})$ using the generating function (33) in (7), avoiding the cumbersome $2d$-dimensional phase space. The construction of the moments from $\psi(t,\boldsymbol{x})$ at a given time t, see the results in (34), takes place exclusively in d-dimensional position space and only involves calculating products of the wave function and its spatial derivates at that particular time t, as well as a final Gaussian spatial filtering with variance ${\sigma_x}^2$. The spatial derivatives as well as the filtering are quasilocal processes and it is sufficient to perform the convolution in a neighborhood of $\boldsymbol{x}$ of size of a few σ_x. The such constructed moments and cumulants approximate those of $\bar{f}$, see (17), and therefore solve the full Boltzmann hierarchy of $\bar{f}$ without any truncation by virtue of (36).

5. Cold initial conditions

The stress tensor T_{ij}, (9c), of a pressureless perfect fluid has the form $T_{ij}^{\mathrm{d}} = \rho_0 n_{\mathrm{d}} a^{-3} u_i^{\mathrm{d}} u_j^{\mathrm{d}}$. The resulting ScM stress tensor T_{ij}^{H} contains an additional contribution Σ_{ij}^{H} which can be interpreted, according to (34f) and (34i), as arising solely from velocity dispersion by virtue of the correspondence $\bar{f} \simeq f_{\mathrm{H}}$ (29). One defining aspect of CDM, that it is initially a pressureless perfect fluid with $\Sigma_{ij}^{\mathrm{d}} = 0$, is not automatically implemented by the ScM. It can however be easily achieved, remembering that if the quantum pressure Q in (25b) is initially small the SPE approximates the dust fluid (10) with arbitrarily precision. The observation that $\nabla_i(n^{\mathrm{H}}\Sigma_{ij}^{\mathrm{H}})$ is proportional to $e^{\frac{{\sigma_x}^2}{2}\Delta}\{n_\psi\nabla_j Q\}$, see [23], therefore shows us how to implement dustlike, and therefore nearly cold initial conditions. To implement cold initial conditions, we thus choose

$$\psi_{\mathrm{ini}}(\boldsymbol{x}) \equiv \sqrt{n_{\mathrm{d}}(t_{\mathrm{ini}},\boldsymbol{x})}\exp\left[\frac{i}{\tilde{\hbar}}\phi_{\mathrm{d}}(t_{\mathrm{ini}},\boldsymbol{x})\right] \tag{37a}$$

$$\text{with} \quad \tilde{\hbar}\text{such that}\boldsymbol{\nabla}Q(t_{\mathrm{ini}},\boldsymbol{x}) \ll \boldsymbol{\nabla}\Phi_\psi(t_{\mathrm{ini}},\boldsymbol{x}), \tag{37b}$$

where $n_{\mathrm{d}}(t_{\mathrm{ini}},\boldsymbol{x})$ and $\phi_{\mathrm{d}}(t_{\mathrm{ini}},\boldsymbol{x})$ are obtained via (10) before shell-crossing and $Q(t_{\mathrm{ini}},\boldsymbol{x})$ and $\Phi_\psi(t_{\mathrm{ini}},\boldsymbol{x})$ are obtained by evaluating (26) and (25d) with $\psi_{\mathrm{ini}}(\boldsymbol{x})$. This choice of $\tilde{\hbar}$ guarantees that $f_{\mathrm{H}}(t_{\mathrm{ini}}) \simeq f(t_{\mathrm{ini}}) = f_{\mathrm{d}}(t_{\mathrm{ini}})$.[15] Note that ScM does not force us to use cold initial conditions and we leave it for the future to investigate ψ_{ini} that correspond to warm initial conditions. We summarize the main features

[15]If $\boldsymbol{\nabla}Q \ll \boldsymbol{\nabla}\Phi_\psi$ everywhere, then f_{H} underestimates the maximal achievable precision with which the SPE can model the dust fluid (10), see [23]. In this case, $f_{\mathrm{naive}} = n_\psi(\boldsymbol{x})\delta_{\mathrm{D}}(\boldsymbol{u} - \boldsymbol{\nabla}\phi(\boldsymbol{x}))$ is closer to f_{d} than f_{H}.

of the ScM and compare them to two other models of CDM in Table I.

III. NUMERICAL IMPLEMENTATION OF THE 2D SCM

In this section, we describe the algorithms used to solve the SPE (21) and the implementation of (34) for constructing the Husimi cumulants by avoiding phase space. The two-dimensional code can be interpreted to describe three-dimensional dynamics in special situations where the wave function is shift symmetric in the z-direction, where $\boldsymbol{x} = (x, y, z)$ are the cartesian coordinates.

A. SPE

For the numerical implementation of the ScM we use a as the time variable, where $da = aHdt$ and H is the Hubble parameter, thus the Schrödinger equation (21a) takes the following form

$$i\tilde{\hbar}\partial_a\psi = -\frac{\tilde{\hbar}^2}{2a^3H}\Delta\psi + \frac{\Phi_\psi}{aH}\psi. \tag{38}$$

Following [18,52,53], we use an alternating direction implicit (ADI) method to discretize and split the single two-dimensional SPE (38) into three equations:

$$e^{-\frac{i\lambda\tilde{\hbar}\epsilon}{4Ha^3}\frac{\partial^2}{\partial x^2}}S(x,y) = e^{\frac{i\lambda\tilde{\hbar}\epsilon}{4Ha^3}\frac{\partial^2}{\partial x^2}}\psi(a,x,y) \tag{39a}$$

$$e^{-\frac{i\lambda\tilde{\hbar}\epsilon}{4Ha^3}\frac{\partial^2}{\partial y^2}}T(x,y) = e^{\frac{i\lambda\tilde{\hbar}\epsilon}{4Ha^3}\frac{\partial^2}{\partial y^2}}S(x,y) \tag{39b}$$

$$e^{\frac{i\lambda\epsilon}{2\tilde{\hbar}Ha}\Phi_\psi}\psi(a+\lambda\epsilon,x,y) = e^{-\frac{i\lambda\epsilon}{2\tilde{\hbar}Ha}\Phi_\psi}T(x,y) \tag{39c}$$

where ϵ is the spatial mesh width of the finite difference mesh, da the temporal step and $\lambda = da/\epsilon$. Then, one can use the central finite difference approximation of third order accuracy

$$\frac{\partial^2 f(x_0)}{\partial x^2} \approx \frac{1}{12\epsilon^2}[-f(x_0-2\epsilon) + 16f(x_0-\epsilon) - 30f(x_0) + 16f(x_0+\epsilon) - f(x_0+2\epsilon)] \tag{40}$$

to replace the second order derivatives in (39). By defining the operator

$$\hat{\delta}_x f(x_0) \equiv -f(x_0-2\epsilon) + 16f(x_0-\epsilon) - 30f(x_0) + 16f(x_0+\epsilon) - f(x_0+2\epsilon), \tag{41}$$

expanding the exponentials to the lowest significant order in ϵ and replacing the continuous variables with discretized notation, we obtain

$$\left(1 - \frac{i\lambda\tilde{\hbar}}{48\epsilon Ha^3}\hat{\delta}_i\right)S_{ij} = \left(1 + \frac{i\lambda\tilde{\hbar}}{48\epsilon Ha^3}\hat{\delta}_i\right)\psi^n_{ij} \tag{42a}$$

$$\left(1 - \frac{i\lambda\tilde{\hbar}}{48\epsilon Ha^3}\hat{\delta}_j\right)T_{ij} = \left(1 + \frac{i\lambda\tilde{\hbar}}{48\epsilon Ha^3}\hat{\delta}_j\right)S_{ij} \tag{42b}$$

$$\left(1 + \frac{i\lambda\epsilon}{2\tilde{\hbar}Ha}\Phi^n_{\psi ij}\right)\psi^{n+1}_{ij} = \left(1 - \frac{i\lambda\epsilon}{2\tilde{\hbar}Ha}\Phi^n_{\psi ij}\right)T_{ij} \tag{42c}$$

where:

$$\psi^n_{ij} = \psi(a_0 + n\lambda\epsilon, x_0 + i\epsilon, y_0 + j\epsilon) = \psi(a,x,y). \tag{43}$$

These difference equations are in the Crank-Nicolson form which guarantees that they are unconditionally stable and they have an error of $\mathcal{O}(\lambda^2\epsilon^2)$ in time and $\mathcal{O}(\epsilon^4)$ in space. Furthermore, the algorithm is manifestly unitary [54], which means that like in a N-body simulation mass conservation is automatic.

We implemented the SPE on a single Nvidia K20X GPU (Kepler architecture) using CUDA C. Due to the memory constraints of the K20X, that is $6GB$ of device memory, we solved (42) with a maximum of 8192^2 points on a regular grid with periodic boundary conditions. Finer resolution is not possible without splitting the full simulation box into regions and either simply copying parts of the simulation box to CPU memory and back, or even more efficiently, using multiple GPUs with appropriate communication between them on region boundaries. Substantial speed improvement over a single CPU was observed by ensuring minimal communication between the host (CPU) and the device (GPU), making sure that kernels had coalesced access to global device memory and efficiently using the device local memory. More detailed description of our numerical implementation, as well as the study of scaling with simulation size is left for a more dedicated publication.

To advance the wave function $\psi^n_{ij} \to \psi^{n+1}_{ij}$ a single time step, we solved the set of cyclic penta-diagonal linear systems (42) using the very efficient algorithm described in [55]. Note that we did not use the first order accuracy formula for the second order derivatives that was used in [18]. From numerical tests, we found that it was not sufficient to solve (42) accurately enough for our initial conditions, in particular the Layzer-Irvine test, described in the following subsection, failed at significantly earlier times. We also did not use the midpoint value of the potential, $\Phi^{n+1/2}_{\psi,ij}$ in (42), as suggested in [18], since in our case the gravitational potential is very slowly evolving. Indeed, although we solved the Poisson equation at every time step, we found very good agreement even if $\Phi^n_{\psi ij}$ was updated only every 20 time steps. To calculate the gravitational potential, we solved the Poisson equation (21b) in

Fourier space, using the CuFFT[16] implementation of the Fast Fourier Transform (FFT) method with periodic boundary conditions on the same grid.

We remind the reader that the dynamical variables are the real part $\Re(\Psi)$ and imaginary part $\Im(\psi)$ of the wave function ψ. These functions are strongly oscillating but otherwise well behaved, see the top panels of Fig. 2. While the absolute value $|\psi| = \sqrt{n_\psi}$ is also a smooth function, the phase $\phi/\tilde{\hbar}$ is not, see the lower panels of Fig. 2. The phase has singular points precisely at locations at which $n_\psi = 0$. The meaning and importance of these phase singularities is discussed in section V A.

B. Layzer-Irvine test of numerical accuracy

Since our numerical method is manifestly unitary [54], testing whether the total mass

$$M(t) = \rho_0 \int \mathrm{d}^3x |\psi(\boldsymbol{x})|$$

is conserved at all times does not tell us how accurately we solve the SPE. Instead, we consider the total energy per mass (23)

$$E(t) =: K + W \tag{44a}$$

where we defined the kinetic K and potential W energy through

$$K(t) = \frac{\tilde{\hbar}^2}{2a^2} \int \mathrm{d}^3x |\boldsymbol{\nabla}_x \psi(\boldsymbol{x})|^2 \tag{44b}$$

$$W(t) = -\frac{\rho_0 G}{2a} \int \mathrm{d}^3x \mathrm{d}^3x' \frac{|\psi(\boldsymbol{x})|^2 |\psi(\boldsymbol{x}')|^2}{|\boldsymbol{x} - \boldsymbol{x}'|} \tag{44c}$$

$$= \frac{1}{2} \int \mathrm{d}^3x \, \Phi_\psi(t, \boldsymbol{x}) |\psi(\boldsymbol{x})|^2 \tag{44d}$$

where Φ_ψ is the Newtonian potential from (21b). Since $\mathcal{E}$ depends explicitly on time through the scale factor a and $\{E, E\} = 0$ we have

$$\frac{dE}{dt} = \partial_t E. \tag{45}$$

Inserting the expressions for K and W and taking into account that partial time derivatives act only on the scale factor $a(t)$, since $\psi(\boldsymbol{x})$ have to be interpreted as canonical position variables we get

$$\frac{d}{dt}(K + W) = -\frac{\dot{a}}{a}(2K + W). \tag{46}$$

This coincides with the Layzer-Irvine equation [1,20,56,57] because we have the same explicit time dependence in the Hamiltonians for N particles (1) and the Schrödinger field (44). We can rewrite (46) as

$$\frac{d}{da}[aE] = -K(a). \tag{47}$$

Since $K \geq 0$ the energy E decays at least as a^{-1}. We can integrate (46) to define a total conserved energy

$$E_{\mathrm{tot}} := E(t) + E_{\mathrm{exp}}(t),$$
$$E_{\mathrm{exp}} = \int_{a_{\mathrm{ini}}}^{a} \frac{2K(a') + W(a')}{a'} da' \tag{48}$$

where we chose arbitrarliy $E_{\mathrm{tot}}(a_{\mathrm{ini}}) = E(a_{\mathrm{ini}})$. A useful test for the accuracy of numerical integration is thus to check that

$$\delta_{E_{\mathrm{tot}}} \equiv \frac{E_{\mathrm{tot}}(a)}{E(a_{\mathrm{ini}})} - 1 \tag{49}$$

remains close to zero.[17] Because (48) requires to calculate $K(a)$, $W(a)$ at all times, we can alternatively test (47) by numerically evaluating $\frac{d}{da}[aE]$ using a 9-point stencil, to test that

$$\delta_K \equiv \frac{\frac{d}{da}[aE]}{-K(a)} - 1 \tag{50}$$

remains close to zero. Figure 3 shows δ_K for a test simulation of a 2D pancake collapse detailed in Sec. IV A. In the range of times where our comparisons with `ColDICE` were performed ($0.02 < a < 0.088$), δ_K does not deviate from 0 further than 0.1%. During later times δ_K departs further from 0. This happens earlier with decreasing spatial and temporal resolution. By experimenting with the spatial resolution, the derivative approximation scheme, and time resolution we found that spatial resolution and the accuracy of the spatial derivative scheme have the largest impact on the time when δ_K starts to deviate from 0; see Fig. 3.

These findings indicate that the use of adaptive mesh refinement (AMR) is imperative in order for a numerical implementation of the ScM to function as a general-purpose tool. We note that an efficient framework for implementing AMR in three dimentions using GPUs is publicly available.[18] The authors of [49], have used a

[16] See http://docs.nvidia.com/cuda/cufft/index.html.

[17] If wanted the integral to contain only W, we could rewrite (47) as $\frac{d}{da}[a^2 E] = aW(a)$ which leads to F.17 in [20] taking into account that $E_{\mathrm{k}}^{\texttt{ColDICE}} = a^2 K$, $E_{\mathrm{p}}^{\texttt{ColDICE}} = a^2 W$. Note that there is a typo in F.20 which should read $E_{\mathrm{exp}}^{\texttt{ColDICE}} = -\int_0^a \frac{1}{a'} E_{\mathrm{p}}(a') da'$.

[18] `GAMER` is available at http://iccs.lbl.gov/research/isaac/GAMER_Framework.html.

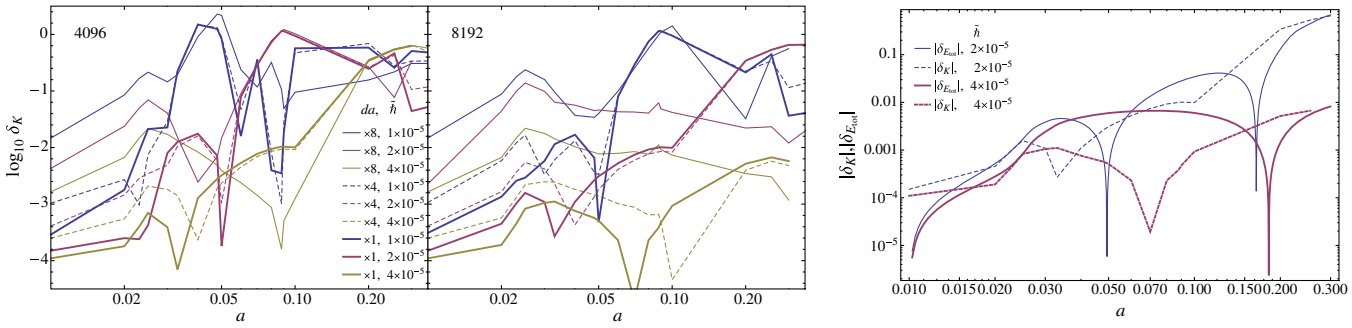

FIG. 3. *Left*: Differential Layzer-Irvine test for the SPE solver for sine initial condition and two different spatial resolutions 4096 (left) and 8192 (right) for three values of da as indicated in the legend (×8 means that da is 8 times larger) and three different values of $\tilde{\hbar}$. The value of A, (50), is calculated from the snapshots of the SPE presented in Sec. IV A. *Right*: Comparison of differential and integrated energy test for the resolution of 8192.

GAMER add-on called ELBDM (extremely light bosonic dark matter) which solves the SpE, however, ELBDM is at present not publicly available.

C. Moments

We use a 9-stencil finite difference method to calculate the spatial gradients entering the expressions for $M^{\mathrm{W}(n)}$ in (34). To obtain the desired Husimi moments $M^{\mathrm{H}(n)}$, we apply a Gaussian filter in an efficient way, described in Appendix B.

D. The choice of $\hbar$

In order to determine the value of $\tilde{\hbar}$ for cold initial conditions, we used the condition (37b) and calculated the $\tilde{\hbar}$-independent number

$$\tilde{Q} = \max_{\boldsymbol{x}}\left(\frac{|\boldsymbol{\nabla} Q(t_{\rm ini},\boldsymbol{x})|}{\tilde{\hbar}^2|\boldsymbol{\nabla}\Phi_\psi(t_{\rm ini},\boldsymbol{x})|}\right), \tag{51}$$

and chosen $\tilde{\hbar}$ such that

$$\tilde{\hbar} \ll \tilde{Q}^{-1/2}. \tag{52}$$

In practice, we cannot choose arbitrary small values of $\tilde{\hbar}$ due numerical limitations: spatial variations of the wave function $|\psi|/|\boldsymbol{\nabla}\psi| \simeq \tilde{\hbar}/|\boldsymbol{\nabla}\phi|$ need to be well resolved by the spatial mesh width ϵ, such that we also require

$$\tilde{\hbar} \gg \epsilon \max_{\boldsymbol{x}}|\boldsymbol{\nabla}\phi(t_{\rm ini},\boldsymbol{x})|. \tag{53}$$

The closer one gets to violating these conditions, the earlier during the time evolution will the quantity δ_K deviate from 0, such that for a given problem the value of $\tilde{\hbar}$ has to be chosen carefully.

IV. TESTS OF THE SCM IN TWO DIMENSIONS

We study two-dimensional cosmological simulations. In terms of three-dimensional space, these simulations can be interpreted as having a phase space density that is shift symmetric in the z direction, where $\boldsymbol{x} = (x, y, z)$, and that vanishes for $u_z \neq 0$, where $\boldsymbol{u} = (u_x, u_y, u_z)$ are the canonical phase space coordinates. Interpreted in three dimensions, this initial condition leads to a filament that extends indefinitely in z-direction. This restriction, although not of much physical relevance, allows us to run two-dimensional simulations with very high resolution with the goal to disentangle any possible failure of the ScM from simple possible numerical inaccuracies.

The theoretical limitation is twofold, while $f_{\rm c}$ would indefinitely produce ever smaller structures in the winding-up phase space sheet, the ScM with a fixed value of $\tilde{\hbar}$ is not able to resolve structures below the phase space scale $\tilde{\hbar}$ even if the SPE were solved exactly. Secondly, even on phase space scales larger than $\tilde{\hbar}$, the coarse-grained CDM dynamics, namely that of $\bar{f}_{\rm c}$, cannot exactly be described by $f^{\rm H}$ since due to (29)

$$\partial_t(f_{\rm H} - \bar{f}_{\rm c}) \simeq \left(\frac{\tilde{\hbar}}{x_{\rm typ}u_{\rm typ}}\right)^2 \frac{\Phi_{\rm H} f_{\rm H}}{x_{\rm typ}u_{\rm typ}},$$

where typical scales, $x_{\rm typ}$ and $u_{\rm typ}$, are the scale on which $f_{\rm H}$ varies most strongly. Because $x_{\rm typ}$ continues to shrink over time as smaller and smaller phase space structures form, the right-hand side might become too large at which point the ScM breaks down. It is this second point that requires a numerical proof and for this we perform a detailed comparison with the publicly available code ColDICE which solves the Vlasov equation (4).

We considered two kinds of cosmological simulations both in a ΛCDM universe where the Hubble parameter is

$$H^2 = H_0^2(\Omega_m a^{-3} + 1 - \Omega_m). \tag{54}$$

The first test is a sine wave collapse, which is a traditional test for N-body codes [58] for which we set $\Omega_m = 1$. The second test uses a Gaussian random field to generate the displacement field, and we chose the value $\Omega_m = 0.312$. The translation of the Zel'dovich displacements used to set up the initial conditions in ColDICE into an initial wave function $\psi_{\rm ini}$ is detailed in Appendix A. We have chosen units where $H_0 = G = c = 1$.[19]

A. Sine wave collapse

As we tested the ScM by comparing with ColDICE, we found it convenient to use the same parameters for the initial sine wave and initial integration redshift and units as in the two-dimensional sine wave collapse presented in the ColDICE article [20]. We checked that the initial conditions for ColDICE and the SPE solver agree to better than 0.025%.[20] Therefore, an increasing deviation signals inaccuracies in either of the two codes, or if this can be excluded, fundamental limitations of the ScM. The initial conditions are detailed in App. A 4.

We ran a number of simulations by changing the number of grid points (either 4096^2 or 8192^2 for the same box size), the value of $\tilde{\hbar} = \{1\times10^{-5}, 2\times10^{-5}, 4\times10^{-5}\}$ and the temporal resolution $da/da_{\rm base} = \{1\times, 4\times, 8\times\}$. From this set, we performed numerical accuracy tests in order to decide which simulation to use for our comparison, and at the same time providing a justification. All simulations had the same initial and final times, $a = \{0.01, 0.3\}$ respectively.

1. Accuracy considerations

To make sure our comparison does not suffer from numerical inaccuracies, we employed the Layzer-Irvine test (50) for deciding until which time the SPE solver may be trusted. For the particular initial conditions chosen we may observe in Fig. 3 that the numerical SPE solution may be trusted until $a = 0.1$ for the simulation with 4096^2 spatial grid points and up to $a = 0.3$ for the 8192^2 grid. In both cases, only the simulations with the largest considered value of $\tilde{\hbar}$ are accurate enough, that is $\tilde{\hbar} = 4\times10^{-5}$ Mpc. Simulations with smaller values of $\tilde{\hbar}$ would need finer spatial resolution, that is, a larger grid of points. Hence, we chose for our comparisons the simulation with $\tilde{\hbar} = 4\times10^{-5}$ Mpc and 8192^2 where the differential energy test (50) is satisfied to better than 0.1% for $a < 0.1$. For this simulation one can expect that any deviations between the coarse-grained moments of ColDICE and the corresponding ones from the ScM can be attributed to a failure of the ScM due to (29), rather than numerical inaccuracy and thus constitutes a test of the ScM. In the right panel of Fig. 3, we show that the differential energy test δ_K (50), that can be applied to single snapshots, is a good indicator for the full energy test $\delta_{E_{\rm tot}}$ (49), that requires evaluation of K and W at each time step during numerical integration of the SPE.

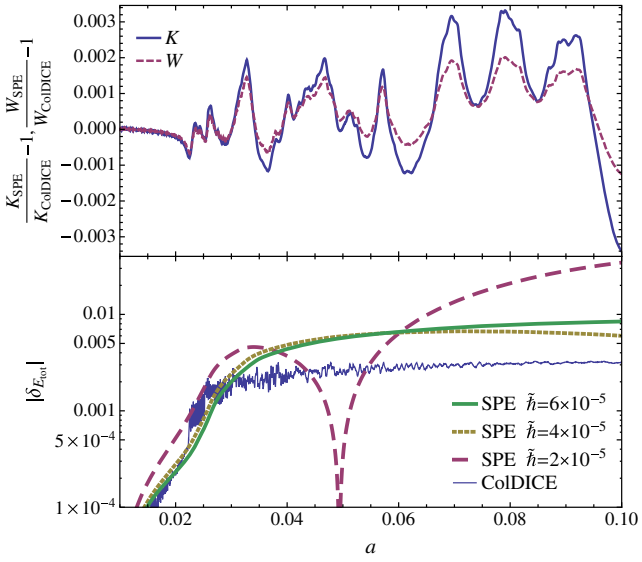

FIG. 4. *Upper panel*: Comparison of the kinetic (K) and potential (W) energy as obtained by ColDICE and the SPE solver with parameters as described in the text. *Lower panel*: Comparison of the total energy test between ColDICE (thin blue) and the SPE solver with settings as described in the text (dashed), together with two other SPE solutions which differ only be the choice of $\tilde{\hbar}$.

We used the publicly available code ColDICE to solve the Vlasov equation (4) for $f_{\rm c}(\boldsymbol{x},\boldsymbol{u})$ and to calculate $n(\boldsymbol{x}) = M^{{\rm c}(0)}(\boldsymbol{x})$, $M_i^{{\rm c}(1)}(\boldsymbol{x})$, and $M_{ij}^{{\rm c}(2)}(\boldsymbol{x})$ from it.[21] These quantities were then coarse grained according to (17) with the same values of σ_x and $\sigma_u = \tilde{\hbar}/(2\sigma_x)$ used in the ScM and then compared to $n^{\rm H}(\boldsymbol{x})$, $M_i^{{\rm H}(1)}(\boldsymbol{x})$ and $M_{ij}^{{\rm H}(2)}(\boldsymbol{x})$, (27) and (34), with ψ satisfying the SPE (21). We ran ColDICE with a precision setting for the invariant threshold[22] $\epsilon_I = 10^{-8}$, and a force resolution grid with 1024^2 pixels, for which equation (48) is satisfied to better than 0.2%, see the thin jagged curve Fig. 4. It it thus justified to take the output of ColDICE to represent $f_{\rm c}$, (14) and its moments (15).

A comparison of K and W between ColDICE and our SPE solver is shown in the upper panel of Fig. 4. The agreement between the codes is better than 0.2% in the

[19]Such that we measure length in units of $H_0^{-1}c$, time in units of H_0^{-1} and mass in units of $H_0^{-1}c^3/G$.

[20]In the sense that $n(a_{\rm ini},x,y)/n_\psi(a_{\rm ini},x,y)-1$, $u_x(a_{\rm ini},x,y)/\partial_x\phi(a_{\rm ini},x,y)-1$ as well as the y component of the velocity agree better than 2.5×10^{-4}. Note this test is nontrivial as it involves the extraction of $M^{{\rm c}(0)}$ and $M^{{\rm c}(1)}$ from the phase space sheet.

[21]To calculate $M_i^{{\rm c}(1)}(\boldsymbol{x})$ and $M_{ij}^{{\rm c}(2)}(\boldsymbol{x})$ from $f_{\rm c}(\boldsymbol{x},\boldsymbol{u})$ we use an add-on for ColDICE that has been kindly provided to us by T. Sousbie.

[22]This number determines the refinement with which the phase space sheet is sampled.

range $0.01 < a < 0.09$ for both variables. In the lower panel, we compare the total energy conservation of ColDICE and the SPE solver for three different values of $\tilde{\hbar}$. We observe that $E_{\rm tot}$ is conserved to a satisfactory level for $\tilde{\hbar} = 4 \times 10^{-5}$ and $\tilde{\hbar} = 6 \times 10^{-5}$, but not so for $\tilde{\hbar} = 2 \times 10^{-5}$, where numerical errors start to accumulate too early in the evolution, causing $\delta_{E_{\rm tot}}$ to change sign around $a = 0.05$. We conclude from Fig. 4 that the SPE is solved with sufficient accuracy such that our subsequent comparison of cumulants $\bar{C}^{{\rm c}(n)}$ and $C^{{\rm H}(n)}$ is a test of the ScM itself, in the sense that observed deviations between $\bar{C}^{{\rm c}(n)}$ and $C^{{\rm H}(n)}$ are not due to numerical inaccuracies in either ColDICE or our SPE solver, but due quantum artifacts discussed in Sec. II E 4.

2. Density

We coarse-grained the output snapshots of the density field $n^{\rm c}(\boldsymbol{x})$ from ColDICE to obtain $\bar{n}^{\rm c}(\boldsymbol{x}) = e^{\frac{\sigma_x^2}{2}\Delta}\{n^{\rm c}\}$. We then compared this to $n^{\rm H}(\boldsymbol{x})$ at various times during the simulation. Based on our discussion in Sec. II E, we expect these quantities to coincide provided we have chosen the same σ_x in the calculation of $n^{\rm H}$ and $\bar{n}^{\rm c}$, chosen a sufficiently small $\tilde{\hbar}$ (37b) and constructed the initial wave function according to (37a).

The top panel (top 3×4 matrix of figures) of Fig. 5 exhibits the results for three snapshots at times $a = 0.023$, $a = 0.033$, and $a = 0.088$, respectively. In the left column, we show $\bar{n}^{\rm c}(\boldsymbol{x})$ of ColDICE, and in the second column $n^{\rm H}(\boldsymbol{x})$, both with $\sigma_x = 0.0035$. In the third and fourth column, we show the fractional difference for $\sigma_x = 0.0035$ and $\sigma_x = 0.006$ respectively. The first snapshot at $a = 0.023$ is taken shortly after the first shell-crossing in the y-direction. By $a = 0.033$ the phase space sheet has wounded round ten times. This process is fully resolved by ColDICE with its adaptive mesh refinement. Although the density is only the projection of the phase space density one can get a feeling for its structure at $a = 0.088$ where several caustics are clearly visible as spherical shells and lobes. The differences between the first and second columns of Fig. 5, i.e. the coarse-grained result of the Vlasov and the ScM solvers respectively, are impossible to discern by eye.

The accuracy by which the ScM code agrees with the coarse-grained Vlasov solver depends on $\tilde{\hbar}$ and σ_x and the integration time $a - a_{\rm ini}$. For fixed $\tilde{\hbar}$ the agreement becomes better if σ_x is increased above a minimal value that avoids interference fringes to become visible. The value of $\sigma_x = 0.0035$ is already slightly too small in order to hide all quantum artifacts. Although they are not visible by eye in the second column, they can be seen when looking at the ratios $\bar{n}^{\rm c}/n^{\rm H} - 1$ in the third column. Increasing the coarse graining scale to $\sigma_x = 0.006$, gives a far better quantitative agreement, at the price of sacrificing some of the small scale structures in the density fields. The fractional difference in the smoothed density field increases from the initial 0.035% to about 10% at the final time for $\sigma_x = 0.006$, or about twice that much for the smaller smoothing scale $\sigma_x = 0.0035$. This seems to be mostly due to small offsets in the positions of high density regions and might have partially a numerical origin. We also tested the larger value $\tilde{\hbar} = 6 \times 10^{-5}$ and found a maximum deviation of 20% at the final time for $\sigma_x = 0.006$.

Since for larger $\tilde{\hbar}$ the numerical accuracy is better, the loss of agreement is likely due to the quantum artifacts of the ScM which can be quantified through the magnitude of $\langle (S^{(3)}_{\tilde{\hbar}ijk})^2\rangle^{1/2}/\langle (S^{(3)}_{{\rm cgV}ijk})^2\rangle^{1/2}$ to test the condition (36a). We plot this quantity for $i = j = k = x$ in the bottom panel of Fig. 7. Comparing this to the upper panel, showing the mean of $\bar{n}^{\rm c}/n^{\rm H} - 1$, we see that there is good correspondence between the scaling of $\langle \bar{n}^{\rm c}/n^{\rm H} - 1\rangle$ with time and $\tilde{\hbar}$ and the corresponding scaling of our measure of quantum artifacts. In order for the ScM to be in good correspondence with the coarse-grained Vlasov equation, we require $|S^{(3)}_{\tilde{\hbar}}| \ll |S^{(3)}_{\rm cgV}|$. We achieve for $\langle (S^{(3)}_{\tilde{\hbar}xxx})^2\rangle^{1/2}/\langle (S^{(3)}_{{\rm cgV}xxx})^2\rangle^{1/2}$ only about 10^{-2} for $\tilde{\hbar} = 4 \times 10^{-5}$ and a factor 10 worse for $\tilde{\hbar} = 6 \times 10^{-5}$. Yet, as can be seen in the upper panel of Fig. 7, for $\tilde{\hbar} = 4 \times 10^{-5}$ and $\sigma_x \geq 0.0035$, we find $\langle \bar{n}^{\rm c}/n^{\rm H} - 1\rangle \lesssim 1\%$ at all times, such that $\langle (S^{(3)}_{\tilde{\hbar}xxx})^2\rangle^{1/2}/\langle (S^{(3)}_{{\rm cgV}xxx})^2\rangle^{1/2} \lesssim 10^{-2}$ seems to indicate acceptable results and allows us to judge whether we approximate the coarse-grained Vlasov from within the ScM.

For even small values of $\tilde{\hbar} < 4 \times 10^{-5}$, the energy test begins to fail, see the dashed curve in the lower panel of Fig. 4. Thus smaller values cause our SPE solver to have too large numerical inaccuracies, while larger values lead to too large quantum artifacts and degrade the accuracy with which the coarse grained Vlasov equation is solved, see the top panel of Fig 7. Hence, for this particular initial condition, SPE integrator and integration time interval, the value $\tilde{\hbar} \simeq 4 \times 10^{-5}$ is optimal.

Note that $|S_{\tilde{\hbar}}| \ll |S_{\rm cgV}|$ only guarantees that the source term for $\partial_t f^{\rm H}(t) - \partial_t \bar{f}(t)$ is small. This implies that, in principle, a nonzero yet small value for that source would always accumulate errors through time evolution so that to make the ScM fail at some point in time.

3. Velocity

We used a code provided to us by T. Sousbie that calculates the first moment $M_i^{{\rm c}(1)}(\boldsymbol{x})$ from the output phase space density of ColDICE. We coarse-grained it, $\bar{M}_i^{{\rm c}(1)}(\boldsymbol{x}) = e^{\frac{\sigma_x^2}{2}\Delta}\{M_i^{{\rm c}(1)}\}$, and constructed the coarse grained velocity field $\bar{u}_i^{\rm c}(\boldsymbol{x}) = \bar{M}_i^{{\rm c}(1)}/\bar{n}$ from it. We split

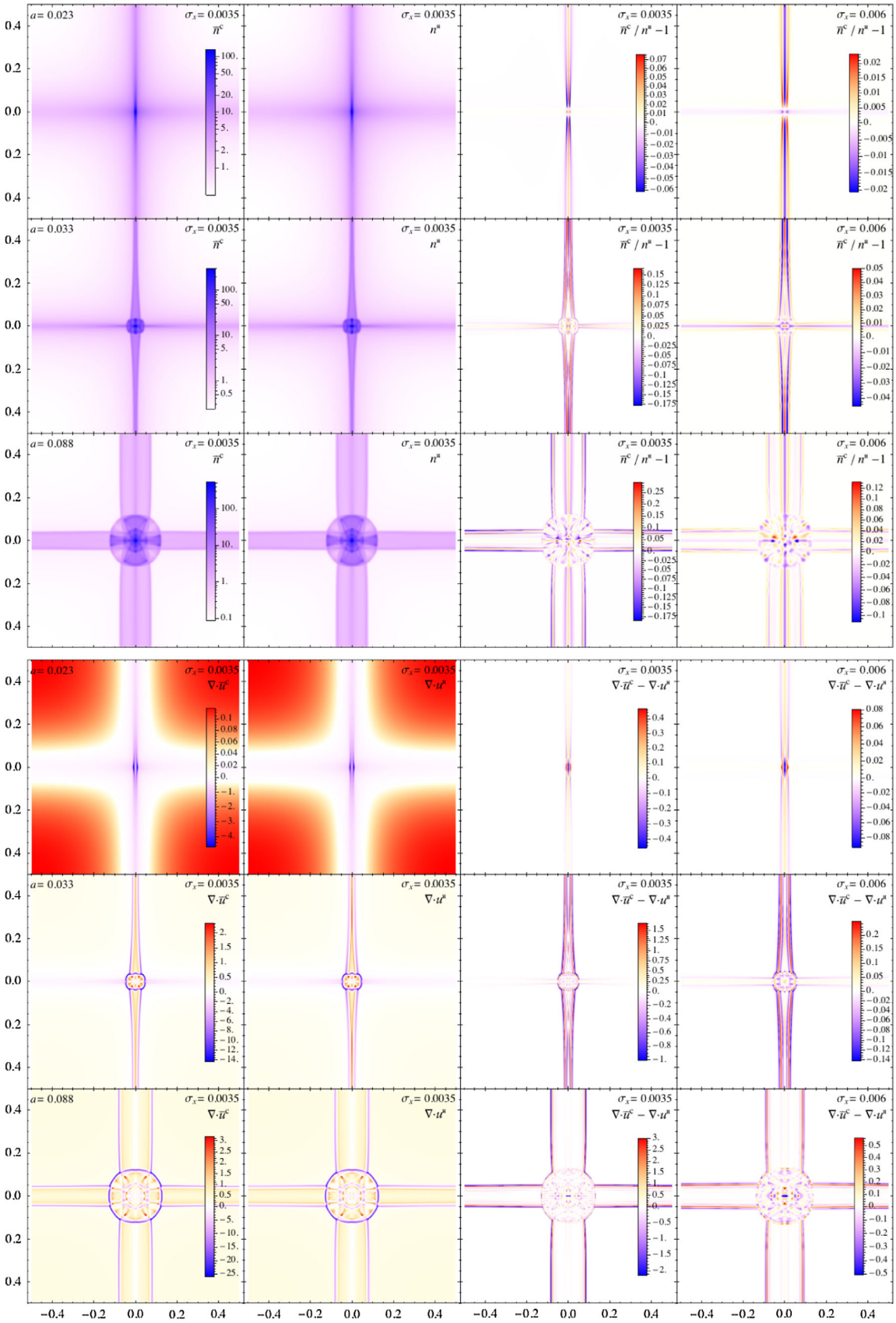

FIG. 5. Sine wave collapse: density (top panel) and velocity divergence (bottom panel) at three different times.

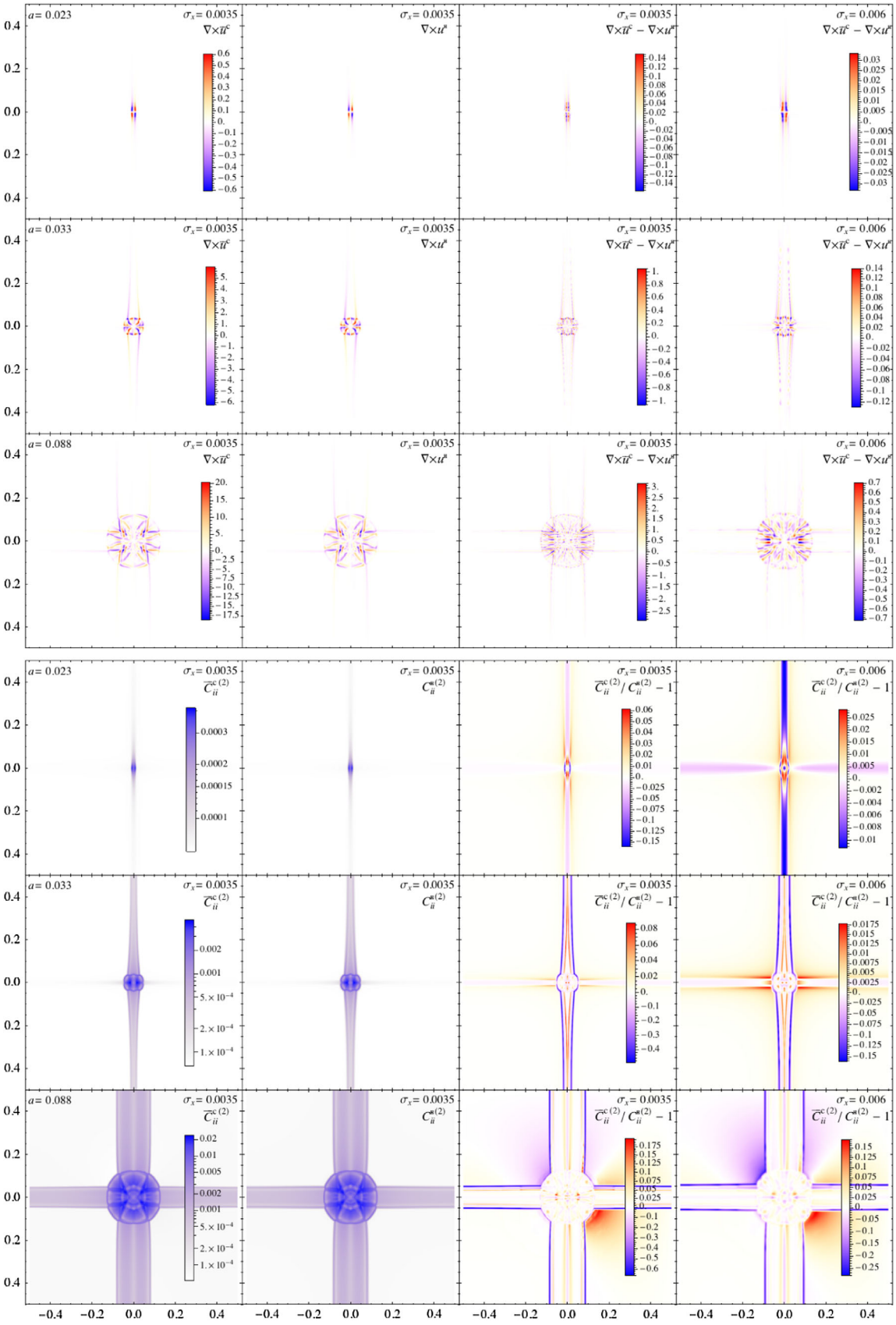

FIG. 6. Sine wave collapse: velocity curl (top panel) and trace of the velocity dispersion (bottom panel) at three different times.

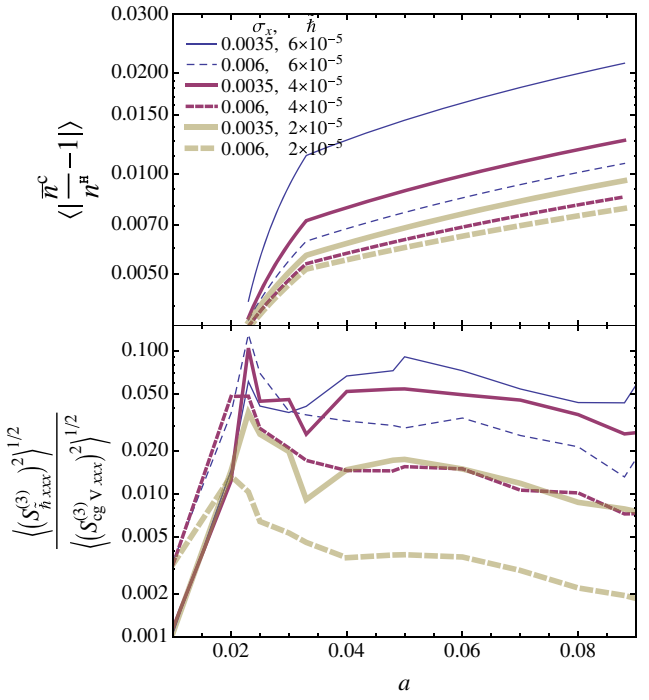

FIG. 7. Upper panel: Mean of the fractional difference of the smoothed density fields $\bar{n}^c$ and n^H as obtained from ColDICE and the ScM, respectively. Lower panel: Testing for quantum artifacts using (36a) for the component $i = j = k = x$ for the same parameters as for the top panel.

the latter into a divergence $\nabla \cdot \bar{\boldsymbol{u}}^c$ and a rotation $\nabla \times \bar{\boldsymbol{u}}^c$ component.

We compare the divergence $\nabla \cdot \bar{\boldsymbol{u}}^c$ obtained from the Vlasov solver ColDICE to that obtained from the ScM in the bottom panel of Fig. 5 for the same three snapshots as with the density. In the left column, we show results of the coarse grained Vlasov, in second that of ScM and in the third and fourth column the difference for $\sigma_x = 0.0035$ and $\sigma_x = 0.006$. The rotation $\nabla \times \bar{\boldsymbol{u}}^c$ has only a nonvanishing z component which we plot in the top panel of Fig. 6. As was the case for the density, we again observe an astonishing visual agreement between the Vlasov code and the ScM for both of these velocity components. Once more, the quantitative agreement for fixed $\tilde{\hbar}$ may be improved by increasing the amount of spatial smoothing as can be seen in the 4th column that compares ScM to Vlasov for a coarse graining scale of $\sigma_x = 0.006$.

It is worth noticing that the wave function with its mere two degrees of freedom is able produce "vorticity without vorticity." What we mean by this is that $\nabla \times \boldsymbol{u}^H$ is nonzero, while the naive estimate of the velocity $\boldsymbol{u}_\psi = \nabla\phi$ has vanishing vorticity. This by itself might not seem surprising as $\boldsymbol{u}^H = e^{\frac{\sigma_x^2}{2}\Delta}\{n_\psi \boldsymbol{u}_\psi\}/n^H$ is the mass-weighted $\boldsymbol{u}_\psi$ and thus trivially has some vorticity. The remarkable aspect of this vorticity is that no extra degree of freedom is necessary to correctly describe the vortical degree of freedom of the velocity field present in the CDM in two dimensions. Although this has been anticipated from our theoretical discussion, this is the first time that it has been actually demonstrated. We discuss this and the microscopic origin of vorticity in the ScM further in Sec. V A. In a similar fashion, despite having only two degrees of freedom in the ScM, all higher Husimi cumulants $C^{H(n)}$ will automatically be present and should agree with their coarse grained Vlasov counterparts $\bar{C}^{c(n)}$.

4. Velocity dispersion

In the bottom panel of Fig. 6, we compare the trace of the velocity dispersion $\bar{C}^{c(2)}_{ii}$ to $C^{H(2)}_{ii}$. The asymmetry seen in the ratios $\bar{C}^{c(2)}_{ii}/C^{H(2)}_{ii}$ is due to ColDICE. We tested that our results are perfectly mirror-symmetric with respect to the axes $x = 0$ and $y = 0$.

B. Gaussian random field

For this test we assumed that the primordial curvature perturbation is a Gaussian random field with a power spectrum generated with the publicly available Boltzmann code CLASS, [59]. We smoothed the matter power spectrum with a Gaussian filter of width 1 Mpc in order to make the numerical evolution better behaved. The erasure of initial power on the smallest scales postpones the occurrence of shell crossings, reducing in turn the amount of necessary refinements in ColDICE and allowing the numerical solution of the SPE to be accurate over longer time periods.

The relation between conventional initial conditions for N-body simulations and the initial wave function $\psi_{\rm ini}(\boldsymbol{x})$ is described in App. A 3. The initial density $M^{c(0)}(t_{\rm ini})$ and velocity fields $M^{c(1)}_i/M^{c(0)}(t_{\rm ini})$ constructed from the ColDICE phase space sheet agree with $n_\psi(t_{\rm ini})$ and $\nabla_i\phi(t_{\rm ini})$ better than 0.01%.

We followed the evolution from $a_{\rm ini} = 1/51 \simeq 0.0196$ to $a = 1$. We present here the first snapshot at $a = 0.02$ shortly after the start of the simulation and at $a = 1$, the final time. The results for $\tilde{\hbar} = 5 \times 10^{-10}$ are shown in Fig. 8. The maximal value of the fractional difference in the smoothed density field increases from 0.01% to about 10% at the final time for $\sigma_x = 0.006L$, or about twice that for the smaller smoothing scale $\sigma_x = 0.0035L$. This seems to be mostly due to small offsets in the positions of high density regions and might partially have numerical origin.

We also tested the larger value $\tilde{\hbar} = 10^{-9}$ and found a maximum deviation of 20% at the final time for $\sigma_x = 0.006L$. Since for larger $\tilde{\hbar}$ the numerical accuracy is better, the loss of agreement is due the degrading of the ScM with increasing $\tilde{\hbar}$, reflected in an increased value of quantum artifacts $S_{\tilde{\hbar}}/S_{\rm cgV}$. For the Gaussian random field we found values of $\langle(S^{(3)}_{\tilde{\hbar}xxx})^2\rangle^{1/2}/\langle(S^{(3)}_{{\rm cgV}xxx})^2\rangle^{1/2} \simeq 10^{-2}$ for $\tilde{\hbar} = 5 \times 10^{-10}$ and about 0.05 for $\tilde{\hbar} = 1 \times 10^{-9}$, which

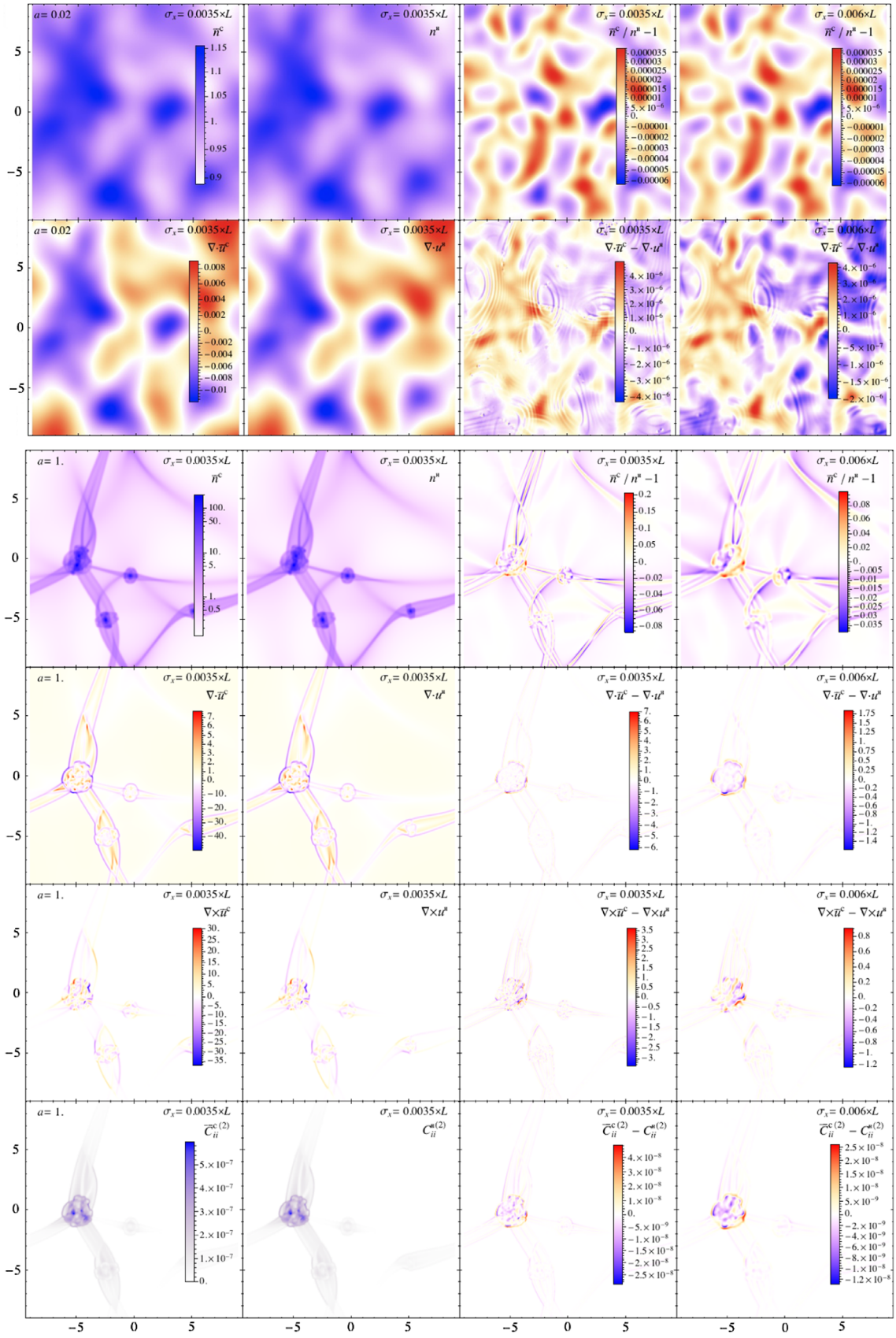

FIG. 8. Gaussian random field collapse: Top two panels at $a = 0.02$ shortly after initial time $a_{\rm ini} = 1/51$, lower panels at $a = 1$.

are very similar to the sine collapse. For smaller $\tilde{\hbar} < 5 \times 10^{-10}$ the energy test failed before the end of the simulation so that the optimal value of $\tilde{\hbar}$ is $\sim 5 \times 10^{-10}$ for this particular set of simulation parameters and initial conditions. For this value and $\sigma_x \geq 0.0035L$, we find $\langle \bar{n}^{\mathrm{c}}/n^{\mathrm{H}} - 1 \rangle < 1\%$ at all times.

We conclude that the ScM can be successfully used to solve the coarse-grained Vlasov equation. The accuracy of that solution is driven by $\tilde{\hbar}$. Joint optimization of $|S^{(3)}_{\tilde{\hbar}}| \ll |S^{(3)}_{\mathrm{cgV}}|$ and $|\delta_{E_{\mathrm{tot}}}| \ll 1$ lead to an optimal value of $\tilde{\hbar}$.

V. DISCUSSION

A. Vorticity without vorticity

It might appear surprising how the two degrees of freedom contained in the wave function include vorticity. First of all, vorticity is not associated with a new degree of freedom, in contrast to CDM where vorticity is a degree of freedom that cannot be constructed from density and velocity divergence, since it is a multistream phenomenon [60–62], and moreover satisfies its own equation of motion. Second, the coarse-grained velocity $\boldsymbol{u}_{\mathrm{H}} = e^{\frac{1}{2}\sigma_x{}^2\Delta}\{n_\psi \boldsymbol{\nabla}\phi\}/n_{\mathrm{H}}$, has some trivial vorticity due to the involved coarse graining which can be seen by rewriting the smoothing as

$$n^{\mathrm{H}}\boldsymbol{u}_{\mathrm{H}} = n^{\mathrm{H}} \exp\left(\sigma_x{}^2 \overleftarrow{\boldsymbol{\nabla}}_x \vec{\boldsymbol{\nabla}}_x\right) \boldsymbol{\nabla}\bar{\phi}, \tag{55}$$

where $\bar{\phi} = e^{\frac{1}{2}\sigma_x{}^2\Delta}\phi$ is the coarse-grained phase. Taylor expanding $\boldsymbol{\nabla} \times \boldsymbol{u}_{\mathrm{H}}$ to leading order in $\sigma_x{}^2$ and using that

$$\boldsymbol{\nabla} \times (\boldsymbol{\nabla}\phi) = 0 \tag{56}$$

we find

$$(\boldsymbol{\nabla} \times \boldsymbol{u}_{\mathrm{H}})_i = \sigma_x^2 \left(\boldsymbol{\nabla} \frac{n^{\mathrm{H}}_{,i}}{n^{\mathrm{H}}} \times \boldsymbol{\nabla}\bar{\phi}_{,i} \right), \tag{57}$$

suggesting that the vorticity is a purely smoothing related byproduct in contrast to CDM where $\boldsymbol{\nabla} \times \boldsymbol{u}_{\mathrm{c}}$ has a component that survives the limit $\sigma_x \to 0$ given by the above mentioned vortical degree of freedom. However it turns out that the innocent looking (56) is in fact not the whole story and there is indeed a microscopic seed for vorticity in the ScM that survives the limit $\sigma_x \to 0$.

The right-hand side of (56) does not vanish in general if the phase has singular gradients $\boldsymbol{\nabla}\phi$ which is known to generally appear during time evolution [23]. If a closed curve C with unit tangent $\boldsymbol{l}$ encloses a singularity,[23] the circulation

$$\frac{1}{2\pi\tilde{\hbar}} \oint_C \boldsymbol{\nabla}\phi \cdot d\boldsymbol{l} = m \tag{58}$$

is a nonzero integrer m [45,63]. In that case, the right-hand side of (56) consists of a sum of Dirac delta functions positioned at the singularities of the phase, which in two dimensions is given by

$$\boldsymbol{\nabla} \times (\boldsymbol{\nabla}\phi) = \hat{\boldsymbol{z}} 2\pi\tilde{\hbar} \sum_i^{N_{\mathrm{vort}}} m_i \delta_{\mathrm{D}}(\boldsymbol{x}_i), \tag{59}$$

with $\hat{\boldsymbol{z}}$ the unit vector perpendicular to the two dimensional surface [63]. Thus, this contributes to $\boldsymbol{\nabla} \times \boldsymbol{u}_{\mathrm{H}}$ even at zeroth order in σ_x

$$\boldsymbol{\nabla} \times \boldsymbol{u}_{\mathrm{H}} = \hat{\boldsymbol{z}} 2 \frac{\sigma_u}{\sigma_x} \sum_i^{N_{\mathrm{vort}}} m_i e^{\frac{(x-x_i)^2}{2\sigma_x{}^2}} + \mathcal{O}(\sigma_x{}^2), \tag{60}$$

with the $\mathcal{O}(\sigma_x{}^2)$ part given by (57). In practice, it is not necessary to keep track of the creation, motion and merging of quantum vortices located at the $\boldsymbol{x}_i(t)$ as well as the varying of their total number $N_{\mathrm{vort}}(t)$ and their individual winding numbers $m_i(t)$: the real and imaginary part of ψ encode these objects but the vortices are not independent vortical degrees of freedom.

In Fig. 9, we show that vortices are identified with phase singularities, which in turn are identified with zeros of the amplitude. The first panel shows in dashed and dotted the zeros of $\Re(\psi)$ and $\Im(\psi)$. Points where both types of zeros (zeros of $\Re(\psi)$ and $\Im(\psi)$) cross are places where ψ is also zero. We mark the zeros of ψ with ellipses. Drawing the same ellipses on the right panel of Fig. 9, that is the plot of the phase $\phi/\tilde{\hbar}$, we observe that all these points carry nonzero circulation with precisely $|m| = 1$. Color and orientation denote the sign of m, with blue/horizontal $m = -1$ and red/vertical $m = 1$.

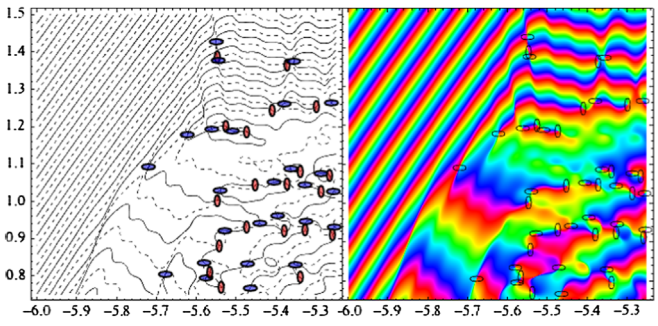

FIG. 9. The solid curves show the zeros of $\Re(\psi)$ and dashed curves the zeros of $\Im(\psi)$. $\Re(\psi)$ and $\Im(\psi)$ are depicted in Fig. 2 upper panels. The zeros of ψ are the crossing of both types and encircled by ellipses. The same ellipses are shown on to right panel, which is a reproduction of Fig. 2 showing the phase $\phi/\tilde{\hbar}$ the wave function. The color and orientation of the ellipses correspond to the orientation of the circulation: blue/horizontal (red/vertical) corresponds to negative (positive) winding number.

[23] In two dimensions, they are pointlike whereas in three dimension they are linelike and thus a network of vortex lines will form for $d = 3$. In one dimension, although pointlike phase gradient singularities arise, as shown in [23], they are not persistent in the sense that they appear only at isolated points in time at which the phase jumps by 2π.

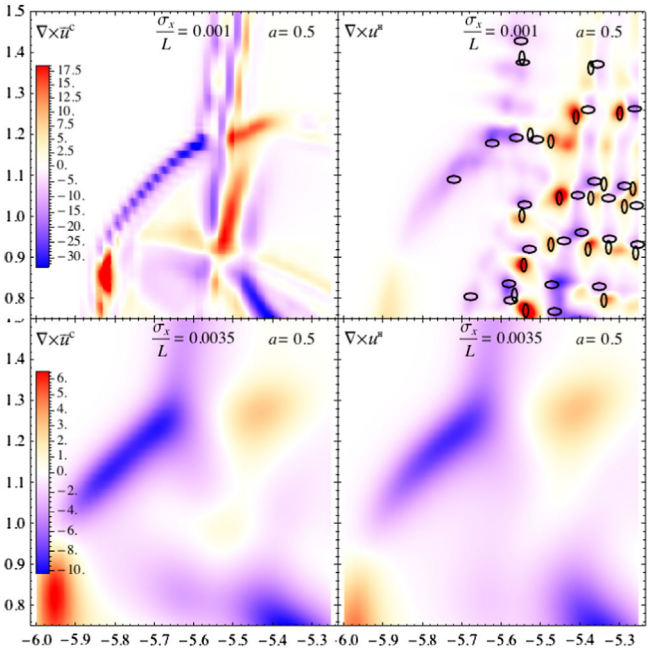

FIG. 10. Coarse-grained vorticity. Upper panels are for $\sigma_x = 0.001 \times 20$ Mpc $= 0.02$ Mpc, lower panels for $\sigma_x = 0.0035 \times 20$ Mpc $= 0.07$ Mpc. Left panels show the results of ColdDICE, right panels those of the ScM. Overplotted on the right are the locations of the vortices identified in Fig. 9.

In Fig. 10, we overplot the vortices on the coarse-grained vorticity obtained by the ScM. In the top panel, we use a very small smoothing scale, which is clearly too small to be in good correspondence with the CDM one shown on the left. However, it clarifies that reducing σ_x to ever smaller values makes $\boldsymbol{\nabla}\times\boldsymbol{u}^{\rm H}$ more and more dominated by the vortices (57), whereas letting σ_x to flow to large enough values that give good correspondence to the coarse-grained CDM, the vortices are not visible and loose their apparent correlation with $\boldsymbol{\nabla}\times\boldsymbol{u}^{\rm H}$. This is yet another variation of our general theme that CDM and ScM are very different UV-completions of the dust fluid, but that once UV physics is smeared out sufficiently, the two theories are in direct correspondence with each other.

B. Pressure of CDM, EFTofLSS and backreaction

The stress tensor is given by $T_{ij} = \rho_0 \bar{M}^{(2)}_{ij}/a^3$ which vanishes in linear perturbation theory $T_{ij} = 0$, such that we can interpret $T^i{}_i = \rho_0 M^{(2)}_{ii}/a^5 = 2P_{\rm eff}$ as the effective pressure $P_{\rm eff}$ [64].[24]

[24]In the effective stress tensor $\tau^i{}_j$, (3.26) of [64], one should replace $\rho v_i v_j$ by $T^i{}_j$ at the right-hand side, see footnote 15 of [64]. The effective stress tensor $\tau^i{}_j$ contains also gradients of the Newtonian potential. These terms cancel however in the two-dimensional trace that we consider here, such that $\tau^i{}_i = T^i{}_i = 2P_{\rm eff}$.

Furthermore, let us define the effective equation of state as $w_{\rm eff} \equiv P_{\rm eff} a^3/\rho_0$ such that, when applied to quantities smoothed in phase space we get

$$\bar{w}_{\rm eff} = a^{-2}(\bar{M}^{(2)}_{ii} - 2\sigma_u{}^2\bar{n})/2, \tag{61}$$

and analogously for $w^{\rm H}_{\rm eff}$. We subtract the 'trivial' part given by $\sigma_u{}^2\bar{n}$, since the effective field theory of large scale structure (EFTofLSS), usually involves only spatial averages. The cosmological average value $\langle\bar{w}_{\rm eff}\rangle$ that we measure from the Vlasov and Schrödinger simulations as a function of time gives us an estimate of backreaction on the cosmological background using the second Friedmann equation

$$3H^2_{\rm eff} + 2\dot{H}_{\rm eff} = -8\pi G\langle P_{\rm eff}\rangle + \Lambda. \tag{62}$$

In Fig. 11, we show the time evolution of $\langle w_{\rm eff}\rangle$ for a ΛCDM and Einstein-de Sitter universe. We also compare in both cases ScM (solid) with the direct Vlasov solution (dotted), which agree extremely well. Furthermore we plot in dashed const $\times (fDaH)^2$, where $f = d\ln D/d\ln a$ and D is the linear growth, which is the estimate for the time dependence of this quantity from perturbation theory. The constant has been fit to match $\langle w_{\rm eff}\rangle$ for $a < 0.1$, where the perturbation theory estimate should be valid.

In Fig. 12, we compare the result of integrating (62) with and without $\langle P_{\rm eff}\rangle$. We denote the result $H_{\rm eff}$ when including $\langle P_{\rm eff}\rangle$ and the standard ΛCDM Hubble parameter (54) by H which is a solution to (62) without $\langle P_{\rm eff}\rangle$. We find that the backreaction on the expansion is a small and a likely a negligible effect.

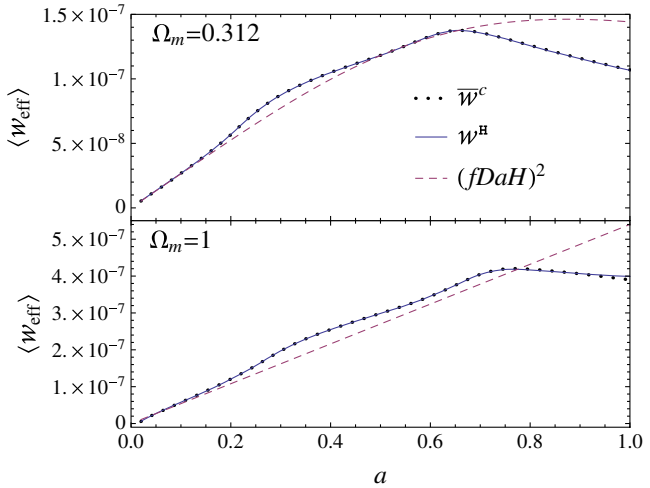

FIG. 11. Effective CDM background equation of state (61). Dotted curves show the result from the Vlasov solver, the solid curve that of the ScM. The dashed curve shows the time dependence suggested by simple perturbative estimates within the EFTofLSS. The upper and lower panel show the result for different cosmologies.

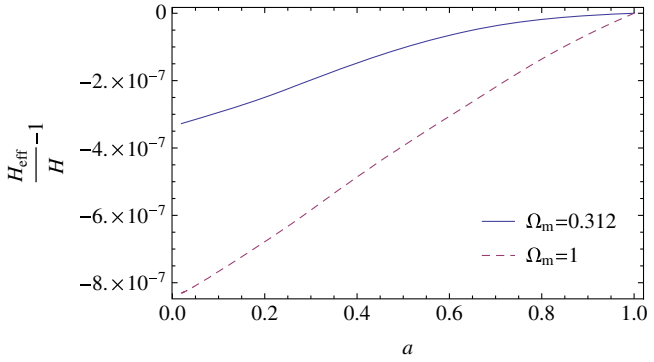

FIG. 12. Comparison of the time evolution of $H(a)$ and $H_{\rm eff}(a)$ for the different cosmologies shown in Fig. 11.

We observe in Fig. 11 that $w_{\rm eff}$ as calculated from the UV complete Vlasov equation is the same as the one from the UV complete ScM. This exemplifies once more that the two degrees of freedom contained in the complex wave function which in the IR are simply related to those of the dust fluid can be used to derive parameters entering an effective field theory of large scale structure (EFTofLSS) based on the ScM. Hence such an EFTofLSS based on the ScM will not require operators associated with missing small scale physics and the field theory itself can be used to measure or derive its EFT parameters.

C. Entropy production in LSS formation

Lynden-Bell suggested in his seminal work [41] that the entropy functional of the coarse-grained phase space density $\bar{f}$ can be used to understand the virialization process as "violent relaxation" and the resulting states as those maximizing the entropy functional. Since the ScM offers an approximation to $\bar{f}$ it is interesting to study the entropy density $s(\boldsymbol{x})$ and entropy S of $f^{\rm H}$, which can be defined respectively as

$$s(\boldsymbol{x}) = -\frac{1}{{\sigma_x}^d}\int \mathrm{d}^d u f_{\rm H} \ln\left[f_{\rm H}{\sigma_u}^d\right]$$
$$S = \int \mathrm{d}^d x s(\boldsymbol{x}). \tag{63}$$

Another interesting quantity is the Massieu function [65]

$$J = S - \frac{\delta S}{\delta E}E, \tag{64}$$

closely related to the free energy $F = -(\frac{\delta S}{\delta E})^{-1}J$ and temperature $T \equiv (\frac{\delta S}{\delta E})^{-1}$ in thermal systems. We expect S and J to increase until virialization ends when a quasiequilibrium state is reached for which S and J are extremized. There are no truly stationary states for self-gravitating systems[25] but only long-lived quasistationary states [68]. The free energy functional was also used in [68–70] to study nonequilibrium phase transitions in systems with long range interactions like gravity. We leave investigating the entropy functional for a future work.

VI. CONCLUSION AND PROSPECTS

We showed that the Schrödinger method (ScM) can be used to solve the Vlasov equation in $d = 2$ dimensions by comparing our ScM code to the state of the art Vlasov code `ColDICE`, see Figs. 5 and 6. We found excellent agreement between the two methods in the cases where an agreement was expected for the ScM to work.

The advantages of the ScM over standard methods of solving the Vlasov equation are:

(i) the information about the phase space distribution in $2d$ dimensions is compressed in a complex wave function in the d dimensions of Eulerian space.
(ii) The moments of the phase space density, which are of direct relevance for observations, can be constructed from the wave function without dealing with the complications of the $2d$-dimensional phase space.

This procedure is summarized in Sec II E 4 and comprises the definition of the ScM as used in this article.

Another difference compared to conventional methods that solve the Vlasov equation is that the ScM approximates the coarse-grained Vlasov equation with fixed phase space resolution. N-body simulations usually have phase space resolutions that depend on time and position in the simulation box as the phase space density is sampled by the clustering particles. In particular, for applications ranging from ray tracing through the simulations, measurement of topological properties of the cosmic web, evaluation of entropy density, or the extraction of metric components, a constant spatial resolution could be a desirable feature. Furthermore, for applications regarding voids or warm initial conditions, which are naturally poorly sampled by N-body simulations, the ScM with its constant resolution might be advantageous.

Another attractive feature of the ScM is that the wave function is a UV completion of the dust fluid [23], in the sense that two degrees of freedom $n_{\rm d}(t,\boldsymbol{x}), \phi_{\rm d}(t,\boldsymbol{x})$ that run into infinities and thus cannot describe CDM in the UV, are replaced by $\psi(t,\boldsymbol{x})$, again 2 degrees of freedom that are finite in the UV and contain all the physics. More importantly, once the finite UV behavior is coarse grained over, the ScM produces an approximate solution to the Vlasov equation. This means that an effective field theory

[25]There are stable configurations for the SPE [42,66,67], but these are purely quantum pressure supported and deep in the regime where the ScM and the right-hand side of (29) can no longer be expanded in powers of $\tilde{\hbar}$, such that the correspondence between $\bar{f}$ and $f_{\rm H}$ is lost.

of large scale structure (EFTofLSS) based on $n_{\rm d}(t,\boldsymbol{x}), \phi_{\rm d}(t,\boldsymbol{x})$ has to introduce operators that take into account the fact that $n_{\rm d}(t,\boldsymbol{x}), \phi_{\rm d}(t,\boldsymbol{x})$ do not actually describe physics in the UV [71]. On the other hand, since $\psi(t,\boldsymbol{x})$ is UV complete, an EFTofLSS based on the ScM, will only require operators that arise through integrating out small scales; the type and number of degrees of freedom does not change. We corroborated that claim in Sec. V B where we measure one parameter of the EFTofLSS $w_{\rm eff}$ within ScM which agrees with the same quantity measured using the Vlasov solver.

We note that replacing the dust energy momentum tensor $T^{\rm d}_{\mu\nu}$ in the formalism explored in [72] by the ScM counterpart $T^{\rm H}_{\mu\nu}$, using (9) and (34) allow a well defined extraction of the non-Newtonian metric quantities like the gravitational slip, vector and tensor perturbations. We leave this for a future study. Further future tests of the ScM may involve warm initial conditions, further investigating vorticity, entropy built-up, extending the method to three-dimensions and in addition implementing adaptive mesh refinement.

ACKNOWLEDGMENTS

We thank Thierry Sousbie for making `ColDICE` publicly available, helping us with the use of `ColDICE` and also for giving us the projection code for obtaining the higher moments from `ColDICE` snapshots. The research leading to these results has received funding from the European Research Council under the European Union's Seventh Framework Programme (FP7/2007-2013)/ERC Grant Agreement n. 617656 "Theories and Models of the Dark Sector: Dark Matter, Dark Energy and Gravity".

APPENDIX A: ZEL'DOVICH INITIAL CONDITIONS

In this Appendix, we describe how we set up the initial conditions for our comparison of ScM and `ColDICE` described in Sec. IV. We use the so-called Zel'dovich approximation (ZA), which is the first order within Lagrangian Perturbation Theory (LPT). For the purpose of comparing two Vlasov solvers, it does not matter that ZA is not as accurate as 2LPT, the second order LPT solution [73,74]. For future applications of the ScM in $d=3$ dimensions, we plan to use `MUSIC` [75], to set up initial conditions with 2LPT.

1. Lagrangian formulation basics

For CDM in the single stream regime, there exists a diffeomorphism between Lagrangian coordinate $\boldsymbol{q}$ of a CDM particle (or dust fluid element) and its Eulerian coordinates

$$\boldsymbol{x} = \boldsymbol{X}(t,\boldsymbol{q}) = \boldsymbol{q} + \boldsymbol{\Psi}(t,\boldsymbol{q}), \tag{A1}$$

where the trajectories $\boldsymbol{X}(t,\boldsymbol{q})$, or alternatively the displacement field $\boldsymbol{\Psi}(\boldsymbol{q},\tau)$, are the integral curves of the Eulerian velocity field

$$\boldsymbol{u}_{\rm d}(\boldsymbol{X}) = \partial_\eta|_q \boldsymbol{\Psi}(\boldsymbol{q}), \tag{A2}$$

where η is superconformal time $a^2 d\eta = a d\tau = dt$. The Jacobian of the coordinate transformation is

$$F_{ij} = \frac{\partial X^i}{\partial q^j} = \delta_{ij} + \partial_{q^j}\Psi_i,$$
$$J_F = \det\left[\delta_{ij} + \partial_{q^j}\Psi_i\right], \tag{A3}$$

and conservation equation (10a) can be integrated exactly to give

$$n_{\rm d}(\boldsymbol{X}) = J_F^{-1}(\boldsymbol{q}). \tag{A4}$$

In order to evaluate $n_{\rm d}$ and $\boldsymbol{u}_{\rm d}$ at the Eulerian position $\boldsymbol{x}$, one has to invert (A1) and express $\boldsymbol{q} = \boldsymbol{Q}(t,\boldsymbol{x})$ and insert this into J_F^{-1} and $\partial_\eta|_q \boldsymbol{\Psi}(\boldsymbol{q})$, respectively.

2. ZA: General initial conditions

In the Zel'dovich approximation, $\boldsymbol{\Psi}(t,\boldsymbol{q})$ separates into

$$\boldsymbol{\Psi} = D(a)\boldsymbol{P}(\boldsymbol{q}) \tag{A5a}$$

with a purely time-dependent linear growth function, with $D(a=0)=0$ and $D(a=1)=1$, as well as a time-independent gradient

$$\boldsymbol{P}(\boldsymbol{q}) = \boldsymbol{\nabla}_q \phi_P(\boldsymbol{q}) \tag{A5b}$$

of some displacement potential $\phi_P(\boldsymbol{q})$. First we explore the consequences of (A5), without taking into account further properties of $\phi_P(\boldsymbol{q})$ and $D(a)$, which will be the subject of the following paragraphs. Relevant for us are expressions for the Eulerian velocity potential $\phi_{\rm d}(\boldsymbol{x})$ and density $n_{\rm d}(\boldsymbol{x})$ as they enter the initial wave function $\psi_{\rm ini}(\boldsymbol{x}) = \sqrt{n_{\rm d}^{\rm ini}}\exp(i\phi_{\rm d}^{\rm ini}/\tilde{\hbar})$. In the remaining section, we approximate $n_{\rm d} = n_{\rm ZA}$ and $\phi_{\rm d} = \phi_{\rm ZA}$, such that the dust solution is initially given by

$$n_{\rm d}(t,\boldsymbol{x}) = \left\{\det\left[\delta_{ij} + D(a)\partial_{q^i}\partial_{q^j}\phi_P(\boldsymbol{q})\right]\right\}^{-1}|_{\boldsymbol{q}=\boldsymbol{Q}(t,\boldsymbol{x})} \tag{A6a}$$

$$\phi_{\rm d}(t,\boldsymbol{x}) = a^2 H f D\left(\phi_P(\boldsymbol{q}) + \frac{1}{2}D(a)|\boldsymbol{P}(\boldsymbol{q})|^2\right)|_{\boldsymbol{q}=\boldsymbol{Q}(t,\boldsymbol{x})}, \tag{A6b}$$

where $f = d\ln D/d\ln a$ is the linear growth rate. The derivation of n_d simply follows by substitution of (A5) into (A3). The Eulerian velocity potential $\phi_{\rm d}$, defined by

$\boldsymbol{u}_{\rm d} = \boldsymbol{\nabla}_x \phi_{\rm d}$, is obtained by first writing the left-hand side of (A2) with the help of (A3) as $\partial_{x^i}\phi_{\rm d} = F^{-1}_{ij}\partial_{q^j}\phi_{\rm d}$ and then multiplying both sides by F_{ki}. Using again (A3) and substituting for $\boldsymbol{\Psi}$ on the right-hand side (A5), the resulting equation for $\partial_{q^k}\phi_{\rm d}$ is

$$\partial_{q^k}\phi_{\rm d} = a^2 H f D(\delta^i_k + D\partial_{q^k}P^i(\boldsymbol{q}))\partial_{q^i}\phi_P(\boldsymbol{q}) \tag{A7}$$

which is a total derivative and can be integrated to give $\phi_{\rm d}(\boldsymbol{q})$ in (A6). The necessary inversion of $\boldsymbol{x} = \boldsymbol{q} + D(a)\boldsymbol{P}(\boldsymbol{q})$ for $\boldsymbol{Q}(t,\boldsymbol{x})$ appearing in (A6) has to be done numerically given the specific $\boldsymbol{P}(\boldsymbol{q})$. We thus use, on the one hand, the field $\phi_P(\boldsymbol{q})$ to create initial amplitude $n^{\rm ini}_{\rm d}(\boldsymbol{x})$ and phase $\phi^{\rm ini}_{\rm d}(\boldsymbol{x})$ of the wave function in Eulerian space, and on the other hand we calculate its gradient (A5) to obtain $\boldsymbol{\Psi}_{\rm ini}(\boldsymbol{q})$ to get the initial Lagrangian displacements (A1) and velocities (A2). The latter are used as the initial conditions for `ColDICE` and requires evaluation of $\boldsymbol{\Psi}_{\rm ini}(\boldsymbol{q})$ on a regular $\boldsymbol{q}$ grid, whereas $n^{\rm ini}_{\rm d}(\boldsymbol{x})$ and $\phi^{\rm ini}_{\rm d}(\boldsymbol{x})$ are evaluated on regular $\boldsymbol{x}$ grid. The such created functions can be turned into an initial wave function $\psi_{\rm ini}(\boldsymbol{x}) = \sqrt{n^{\rm ini}_{\rm d}(\boldsymbol{x})}e^{i\phi^{\rm ini}_{\rm d}(\boldsymbol{x})/\tilde{\hbar}}$ for any value of $\tilde{\hbar}$.

3. ZA: cosmological simulation initial conditions

In the Zel'dovich approximation, $\boldsymbol{\nabla}_q \cdot \boldsymbol{P}(\boldsymbol{q}) = -\delta_{\rm lin}(\boldsymbol{x}=\boldsymbol{q})$ where $\delta_{\rm lin}(\boldsymbol{q})$ is the initial linear density field, linearly extrapolated to $a = 1$. From (10d), it then follows that the velocity potential is a Gaussian random field with power spectrum

$$P_{\phi_P}(k) = \frac{P_{\rm lin}(k, z=0)}{k^4} \tag{A8}$$

where $P_{\rm lin}(k, z = 0)$ is the linear matter power spectrum at $a = 1$. For cosmological simulations $\phi_P(\boldsymbol{q})$ is therefore a Gaussian random field and can be easily generated from $P_{\rm lin}$ which in turn can obtained from Einstein-Boltzmann codes like `class`. We choose the following parameters and units

$$L = 20\ {\rm Mpc} \tag{A9}$$

$$\Omega_m = 0.312046 \tag{A10}$$

$$h = 0.67556 \tag{A11}$$

$$a_{\rm ini} = \frac{1}{51} \tag{A12}$$

Where L is the size of the periodic box. We also apply a Gaussian filter with width $R = 1$ Mpc to the linear power spectrum $\bar{P}_{\rm lin}(k) = P_{\rm lin}(k)e^{-R^2k^2}$ to prevent the formation of structure on very small scales. In order to avoid sampling a three-dimensional $\phi_P(\boldsymbol{q})$ and considering then only some two-dimensional restriction $\phi_P(q_x, q_y, q_z = 0)$ relevant for our two-dimensional simulations, we can directly sample such a two-dimensional realization with the same statistics if we use instead a two-dimensional version of that power spectrum

$$P^{\rm 2D}_{\phi_P}(k) = 2\int_0^\infty {\rm d}p\, \frac{\bar{P}_{\rm lin}(\sqrt{k^2+p^2})}{(k^2+p^2)^2}. \tag{A13}$$

4. ZA: Plane wave initial conditions

For numerical tests, we have assumed instead that $\boldsymbol{P}(\boldsymbol{q})$ consists of three perpendicular sine waves with a periodicity of $2L$ and constant amplitude $\boldsymbol{A}$ such that

$$\phi_P(\boldsymbol{q}) = \sum_{i=1}^{3} A_i \frac{L^2}{\pi^2}\cos\left(\frac{q_i\pi}{L}\right). \tag{A14}$$

The two-dimensional case studied in this article then corresponds to $A_3 = 0$. With this definition (A6) simplify to

$$n_{\rm d}(t,\boldsymbol{x}) = \left\{\prod_{i=1}^{3}\left[1 - D(a)A_i\cos\left(\frac{q_i\pi}{L}\right)\right]\right\}^{-1}\Bigg|_{\boldsymbol{q}=\boldsymbol{Q}(t,\boldsymbol{x})} \tag{A15}$$

$$\phi_{\rm d}(t,\boldsymbol{x}) = a^2 H f D \sum_{i=1}^{3}\left(A_i\frac{L^2}{\pi^2}\cos\left(\frac{q_i\pi}{L}\right) + \frac{1}{2}D(a)\left(A_i\frac{L}{\pi}\sin\left(\frac{q_i\pi}{L}\right)\right)^2\right)\Bigg|_{\boldsymbol{q}=\boldsymbol{Q}(t,\boldsymbol{x})}. \tag{A16}$$

For our two-dimensional setup, we have chosen

$$A^i = (30, 40, 0) \tag{A17}$$

$$L = H_0^{-1}c = 1 \tag{A18}$$

$$\Omega_m = 1 \tag{A19}$$

$$D(a) = a \tag{A20}$$

$$a_{\rm ini} = 0.01 \tag{A21}$$

to match initial conditions presented in [20].

APPENDIX B: GAUSSIAN FILTERING

A convolution of a function f with a filter $W^{(d)}$

$$(W^{(d)} * f)(\boldsymbol{x}) = \int_{L^d} {\rm d}^d x\, x W^{(d)}(\boldsymbol{x}-\boldsymbol{x}', \sigma_x) f(\boldsymbol{x}')$$

in n-dimensional space can be approximated by

$$(W^{(d)} * f)(\boldsymbol{x}) \simeq \int_{\boldsymbol{x}\pm 5\sigma_x} \mathrm{d}^d x W^{(d)}(\boldsymbol{x}-\boldsymbol{x}', \sigma_x) f(\boldsymbol{x}')$$

involving only a neighborhood of a few σ_x around the point of interest $\boldsymbol{x}$, if the filter has an effective support only in a small region $5\sigma_x$ compared to the size L of the periodic space. This makes the filtering process quasilocal and allows a significant speed up by a factor $\frac{10\sigma_x}{L}$ in one dimension. Furthermore, since we use an isotropic Gaussian

$$W^{(d)}(\boldsymbol{x}) = \frac{1}{(2\pi {\sigma_x}^2)^{d/2}} \exp\left(-\frac{|\boldsymbol{x}|^2}{2{\sigma_x}^2}\right)$$

that decomposes like

$$W^{(d)}(\boldsymbol{x}) = W^{(1)}(x^1) * \ldots * W^{(1)}(x^d),$$

we can apply the one-dimensional filter sequentially which again allows a significant speed up such that we reduce the total operations per pixel from the *a priori* N to $\frac{10n\sigma_x}{L} N^{1/d}$, where N is the total number of grid points. For our two-dimensional case with $\sigma_x/L = 0.0035$ and $N = 8192^2$, we reduce the number of computations by a factor 0.4×10^{-5}.

APPENDIX C: ONE-DIMENSIONAL PANCAKE COLLAPSE

In this section, we extend the analysis of Appendix B of [23] for the one-dimensional pancake collapse [58,76–79]. In [23], the "Bohmian" trajectories, the closest analogy to the concept of trajectories that exists in the ScM, was compared only to ZA trajectories. Here we also compare it to CDM. We also focus on the difference between ZA and CDM, suggesting a straightforward algorithm to improve the ZA beyond the occurrence of shell crossing.

For plane-parallel initial conditions

$$\boldsymbol{X}(t, \boldsymbol{q}) =: (X(t,q), q_y, q_z)$$

and $\boldsymbol{q} =: (q, q_y, q_z)$. Without loss of generality we consider the trajectories $(X(t,q), 0, 0)$ such that (12) becomes

$$\ddot{X}(q) = G\rho_0 a \int \mathrm{d}q' \mathrm{d}q'_y \mathrm{d}q'_z \left\{ \frac{X(q)-q'}{[(X(q)-q')^2 + {q'_y}^2 + {q'_z}^2]^{3/2}} - \frac{X(q)-X(q')}{[(X(q)-X(q'))^2 + {q'_y}^2 + {q'_z}^2]^{3/2}} \right\}, \tag{C1}$$

where $d\eta = a^2 dt$ is superconformal time and the dot denotes throughout this section a derivative with respect to η rather than t. Performing the q'_y and q'_z integrals gives

$$\ddot{X}(q) = 2\pi G\rho_0 a \int \mathrm{d}q' [\mathrm{sgn}(X(q)-q') - \mathrm{sgn}(X(q)-X(q'))], \tag{C2}$$

where sgn is 1 if the argument is positive, -1 if it is negative and 0 if the argument vanishes. The first integral can be performed and we arrive at

$$\ddot{X}(q) = 4\pi G\rho_0 a \left\{ X(q) - \frac{1}{2}\int \mathrm{d}q' \mathrm{sgn}[X(q)-X(q')] \right\} \tag{C3}$$

Before shell-crossing, that is, before any q' other than q exists such that $X(q) = X(q')$, the quantity $\mathrm{sgn}(X(q) - X(q'))$ is constant in time and therefore equals $\mathrm{sgn}(q-q')$. Then the second term can be integrated and we obtain

$$\ddot{\Psi}^{\mathrm{ZA}}(q) = 4\pi G\rho_0 a \Psi^{\mathrm{ZA}}(q), \tag{C4}$$

where we used the displacement field $\Psi(q) \equiv X(q) - q$ and attached the label ZA to make clear that the solution to (C4) is the Zel'dovich approximation.[26] We can rewrite (C3) in terms of Ψ

$$\ddot{\Psi}(q) = 4\pi G\rho_0 a(\Psi(q) + g[\Psi](q)))$$
$$g[\Psi](q) = q - \frac{1}{2}\int \mathrm{d}q' \mathrm{sgn}(X(q)-X(q')) \tag{C5}$$

which makes it manifest that before shell-crossing, when g identically vanishes, we recover the ZA, but once CDM undergoes shell-crossing and mixing, g becomes nonzero and the ZA is no longer a solution to (C5).

We could have also arrived to (C4) following the standard treatment of the Lagrangian formulation of CDM that assumes the existence of the inverse of $\partial_{q^i} X^j$ and makes use of it, see i.e. App. B of [23] or [39]. Such an assumption, however, does exclude the multistream regime from the outset and is therefore useless for our purposes. We thus see that the g-term missing in the Zel'dovich approximation is the "glue" that distinguishes the dispersing and physically wrong behavior of the ZA trajectories (red dotted) from those of CDM (yellow thick) in the upper panel of Fig. 13. To solve (C5) we discretized the equation using 512 particles. An alternative method that relies on piecewise analytic solutions has been proposed and employed in one-dimensional simulations in [77–79].

In the lower panel, we reproduced Fig. 8 from [23] showing the Bohmian trajectories, the integral curves of the $\nabla\phi(t,\boldsymbol{x})$, overplotted with CDM trajectories. Note that although the Bohmian trajectories approximate those of the ZA before shell crossing and stick together in a similar

[26] It is an approximation to (12) in three dimensions and arises in Lagrangian perturbation theory. Only before shell-crossing $\Psi^{\mathrm{ZA}}(q)$ is the exact solution in the one-dimensional case.

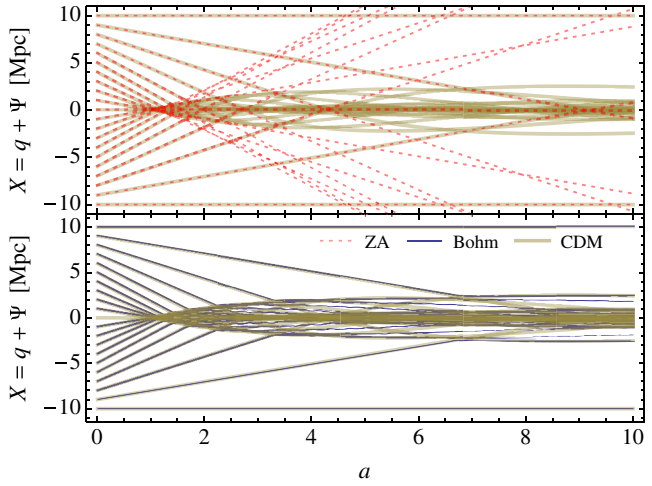

FIG. 13. Upper panel: *red dotted* Zel'dovich trajectories (C4) and *thick yellow* CDM trajectories (C5). Lower panel: blue Bohmian trajectories (B2) of [23] *thick yellow* CDM trajectories (C5).

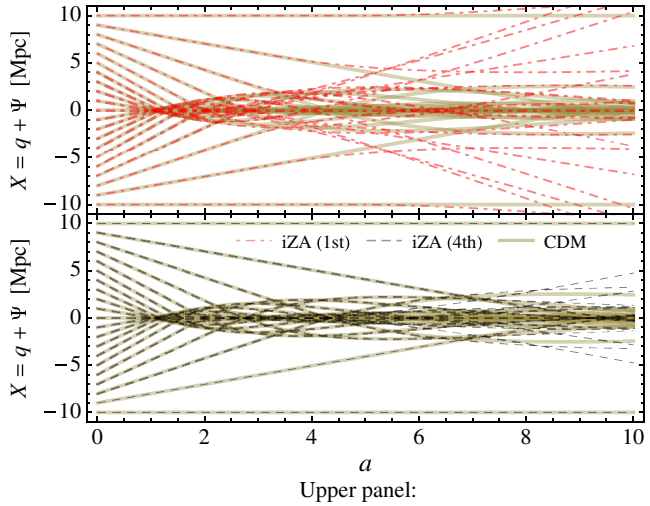

FIG. 14. *Red dot-dashed* is the first iteration of the iZA, (C5) solved with fixed $g[\Psi^{\mathrm{ZA}}]$. Lower panel: *black dashed* is fourth iteration of the iZA, (C5) solved with fixed $g[\Psi^{\mathrm{iZa\,(3rd)}}]$. In both panels are the *thick yellow* curves CDM trajectories of (C5).

fashion as CDM after shell crossing, these nonintersecting Bohmian trajectories are not of any direct physical relevance and in particular do not correspond to CDM trajectories after shell-crossing. What the Bohmian trajectories reveal is that the ScM produces "shell-crossing without shell-crossing" in a similar fashion as Newton's cradle allows a ball to apparently cross the center of the cradle.

Since very shortly after shell-crossing Ψ^{ZA} and Ψ do not deviate much from each other it is interesting to investigate an iterated ZA (iZA) in which $g[\Psi]$ in (C5) is replaced by $g[\Psi^{\mathrm{ZA}}]$. This function can be precalculated and stored in an interpolation table $g[\Psi^{\mathrm{ZA}}](t,q)$ such that the now again local equation

$$\ddot{\Psi}^{\mathrm{iZA}(n)}(q) = 4\pi G\rho_0 a(\Psi^{\mathrm{iZA}(n)}(q) + g[\Psi^{\mathrm{iZA}(n-1)}](q)), \tag{C6}$$

where $\Psi^{\mathrm{iZA}(0)} = \Psi^{\mathrm{ZA}}$, can be solved for $\Psi^{\mathrm{iZA\,(1st)}}$. The such obtained $\Psi^{\mathrm{iZA\,(1st)}}$ could then be used to calculate $\Psi^{\mathrm{iZa\,(2nd)}}$, leading to the hierarchy (C6). This iterative scheme to improve the ZA has been suggested before [80], but to our knowledge, has never been explicitly tested. A similar scheme in one dimension has been proposed in [81] and successfully tested [82].

We plot the first and fourth iteration of the iZA in Fig. 14. Each iteration significantly delays the time at which iZA trajectories deviate from CDM in the multistream regime, such that this method indeed seems to converge to CDM. It should be noted that this improvement of the ZA in one dimension is completely independent from any perturbative improvement of the ZA in three dimensions. Indeed, if we expanded (C5) perturbatively, the g-term vanishes at each order in perturbation theory. Nonperturbative corrections mimicking the glue term g have been suggested to improve mock simulations [83–85] and also to improve perturbation theory [86–88]. It would be interesting to investigate whether the iZA is a feasible approach to improve three-dimensional mock simulations or Lagrangian perturbation theory, and how this relates to other Lagrangian schemes that improve the ZA beyond shell-crossing like `COLA` [89,90] and `PINOCCHIO` [91,92]. Recently an approach to calculate statistical quantities of the displacement field based on the CDM (12) has been developed in [93] which does neither assume invertibility of $\partial_{q^i} X^j$ nor a Taylor expansion in Ψ, and thus allows for a proper inclusion of multistreaming effects.

APPENDIX D: DERIVATION OF (12)

The CDM potential is given by

$$\Phi_{\mathrm{c}}(\boldsymbol{x}) = -\frac{G\rho_0}{a}\int \mathrm{d}^3x' \frac{n_{\mathrm{c}}(\boldsymbol{x}') - 1}{|\boldsymbol{x}-\boldsymbol{x}'|} \tag{D1}$$

and its gradient is

$$\boldsymbol{\nabla}_x \Phi_{\mathrm{c}}(\boldsymbol{x}) = \frac{G\rho_0}{a}\int \mathrm{d}^3x' [n_{\mathrm{c}}(\boldsymbol{x}') - 1] \frac{\boldsymbol{x}-\boldsymbol{x}'}{|\boldsymbol{x}-\boldsymbol{x}'|^3}. \tag{D2}$$

We then split the integral into two parts as

$$\boldsymbol{\nabla}_x \Phi_{\mathrm{c}}(\boldsymbol{x}) = \frac{G\rho_0}{a}\left(\int \mathrm{d}^3x' n_{\mathrm{c}}(\boldsymbol{x}') \frac{\boldsymbol{x}-\boldsymbol{x}'}{|\boldsymbol{x}-\boldsymbol{x}'|^3} - \int \mathrm{d}^3q' \frac{\boldsymbol{x}-\boldsymbol{q}'}{|\boldsymbol{x}-\boldsymbol{q}'|^3}\right), \tag{D3}$$

where we simply renamed the dummy variable $\boldsymbol{x}'$ in the second integrand to $\boldsymbol{q}'$. Next, we switch to Lagrangian coordinates in the first integral. One has to be very careful with this variable transformation since it is not a diffeomorphism, because we allow for multistreaming.

We assume that Eulerian space $\mathbb{X} = \bigcup_{\mu=1}^{M} \mathbb{X}_\mu$ can be decomposed into M subsets $\mathbb{X}_\mu$ in each of which $\boldsymbol{X}_\mu$, the restriction of $\boldsymbol{X}$ that takes values in $\mathbb{X}_\mu$, has a fixed number of streams N_μ, neglecting the zero-measure subsets that are the caustics between those regions. Furthermore, the inverse image $\mathbb{Q}_\mu$ in Lagrangian space, defined by $\boldsymbol{X}_\mu(\mathbb{Q}_\mu) = \mathbb{X}_\mu$ decomposes into $\mathbb{Q}_\mu = \bigcup_{\alpha_\mu=1}^{N_\mu} \mathbb{Q}_{\alpha_\mu}$, such that $\boldsymbol{X}_{\alpha_\mu}$, the restriction of $\boldsymbol{X}_\mu$ that has inverse image $\mathbb{Q}_{\alpha_\mu}$, is a diffeomorphism for all α_μ and μ. Therefore, the inverse of $\boldsymbol{X}_{\alpha_\mu}(\boldsymbol{q})$ exists and is denoted by $\boldsymbol{Q}_{\alpha_\mu}(\boldsymbol{x})$.

We now consider the integral

$$\int_{\mathbb{X}} \mathrm{d}^3x n_{\mathrm{c}}(\boldsymbol{x}) h(\boldsymbol{x}) \tag{D4}$$

with some function $h(\boldsymbol{x})$ and split it into the sum of M Eulerian regions with fixed number of streams

$$\sum_{\mu=1}^{M} \int_{\mathbb{X}_\mu} \mathrm{d}^3x n_{\mathrm{c}}(\boldsymbol{x}) h(\boldsymbol{x}). \tag{D5}$$

Next we insert the expression of $n_{\mathrm{c}}(\boldsymbol{x})$ in terms of sum over streams, (15b), such that

$$\sum_{\mu=1}^{M} \sum_{\alpha_\mu=1}^{N_\mu} \int_{\mathbb{X}_\mu} \mathrm{d}^3x h(\boldsymbol{x}) \frac{1}{|\det \partial_{q^i} X^j_{\alpha_\mu}(\boldsymbol{q})|}\bigg|_{\boldsymbol{q}=\boldsymbol{Q}_{\alpha_\mu}(\boldsymbol{x})}, \tag{D6}$$

where we pulled out of the integral the sum over streams. Then we change coordinates from $\boldsymbol{x}$ to $\boldsymbol{q}$ in the integral. In the Lagrangian region $\mathbb{Q}_{\alpha_\mu}$, the volume element transforms as $\mathrm{d}^3x = \mathrm{d}^3q \det(\partial_{q^i} X^j_{\alpha_\mu}(\boldsymbol{q}))$, such that we are left with

$$\sum_{\mu=1}^{M} \sum_{\alpha_\mu=1}^{N_\mu} \int_{\mathbb{Q}_{\alpha_\mu}} \mathrm{d}^3q h(\boldsymbol{X}_{\alpha_\mu}(\boldsymbol{q})) \mathrm{sgn}(\det \partial_{q^i} X^j_{\alpha_\mu}(\boldsymbol{q})). \tag{D7}$$

Next, we push the α_μ-sum back into the integral

$$\sum_{\mu=1}^{M} \int_{\mathbb{Q}_\mu} \mathrm{d}^3q h[\boldsymbol{X}_\mu(\boldsymbol{q})] \sum_{\alpha_\mu=1}^{N_\mu} \mathrm{sgn}(\det \partial_{q^i} X^j_{\alpha_\mu}(\boldsymbol{q})), \tag{D8}$$

after which we pulled out of the sum $h[\boldsymbol{X}_\mu(\boldsymbol{q})]$, since h is a function of $\boldsymbol{x}$ and therefore the same for all α_μ. The function sgn equals 1 if the argument is positive, -1 if it is negative and 0 if the argument vanishes. Since $\boldsymbol{X}(t,\boldsymbol{q})$ belongs to the homotopy class of the identity as $\boldsymbol{X}(t=0,\boldsymbol{q}) = \boldsymbol{q}$, the α_μ-sum in the integral is 1, see § 4 of [38]. We can finally absorb the sum over μ to get the desired result

$$\int_{\mathbb{X}} \mathrm{d}^3x n_{\mathrm{c}}(\boldsymbol{x}) h(\boldsymbol{x}) = \int_{\mathbb{Q}} \mathrm{d}^3q h(\boldsymbol{X}(\boldsymbol{q})). \tag{D9}$$

Applying this result to the first term in (D3) we obtain

$$\boldsymbol{\nabla}_x \Phi_{\mathrm{c}}(\boldsymbol{x}) = \frac{G\rho_0}{a} \int \mathrm{d}^3q' \left(\frac{\boldsymbol{x} - \boldsymbol{X}(t,\boldsymbol{q}')}{|\boldsymbol{x} - \boldsymbol{X}(t,\boldsymbol{q}')|^3} - \frac{\boldsymbol{x} - \boldsymbol{q}'}{|\boldsymbol{x} - \boldsymbol{q}'|^3} \right), \tag{D10}$$

which leads to (12) upon evaluating the gravitational acceleration $-\boldsymbol{\nabla}_x \Phi_{\mathrm{c}}$ at $\boldsymbol{x} = \boldsymbol{X}(t,\boldsymbol{q})$.

APPENDIX E: PROOF THAT f_{c} SATISFIES THE VLASOV EQUATION

Multiply $f_{\mathrm{c}}(t,\boldsymbol{x},\boldsymbol{u})$, (14), by a smooth test function $h(\boldsymbol{u})$ and consider the time derivative of $\int \mathrm{d}^3u f_{\mathrm{c}}(t,\boldsymbol{x},\boldsymbol{u}) h(\boldsymbol{u})$. With the help of (D9) and (12) it is easy to see that f_{c} satisfies the Vlasov equation (4).

APPENDIX F: DIFFERENCES OF PHASE SPACE DISTRIBUTIONS

Here we collect some results from [23] relevant for testing within the ScM, how well the ScM is expected to approximate the coarse-grained Vlasov or the Vlasov equation. The coarse grained Vlasov equation is

$$\partial_t \bar{f} = -\frac{\boldsymbol{u}}{a^2} \boldsymbol{\nabla}_x \bar{f} - \frac{{\sigma_u}^2}{a^2} \boldsymbol{\nabla}_x \boldsymbol{\nabla}_u \bar{f} + \boldsymbol{\nabla}_x \bar{\Phi} \exp({\sigma_x}^2 \overleftarrow{\boldsymbol{\nabla}}_x \vec{\boldsymbol{\nabla}}_x) \boldsymbol{\nabla}_u \bar{f} \tag{F1a}$$

whereas evolution of the Husimi distribution is given by

$$\partial_t f_{\mathrm{H}} = -\frac{\boldsymbol{u}}{a^2} \boldsymbol{\nabla}_x f_{\mathrm{H}} - \frac{{\sigma_u}^2}{a^2} \boldsymbol{\nabla}_x \boldsymbol{\nabla}_u f_{\mathrm{H}} + \Phi_{\mathrm{H}} \exp({\sigma_x}^2 \overleftarrow{\boldsymbol{\nabla}}_x \vec{\boldsymbol{\nabla}}_x) \frac{2}{\tilde{\hbar}} \sin\left(\frac{\tilde{\hbar}}{2} \overleftarrow{\boldsymbol{\nabla}}_x \vec{\boldsymbol{\nabla}}_u \right) f_{\mathrm{H}}. \tag{F2a}$$

If initially $f_{\mathrm{H}}(t_{\mathrm{ini}}) = \bar{f}(t_{\mathrm{ini}})$, then

$$\partial_t (f_{\mathrm{H}} - \bar{f})_{\mathrm{ini}} = \Phi_{\mathrm{H}}(t_{\mathrm{ini}}) \exp({\sigma_x}^2 \overleftarrow{\boldsymbol{\nabla}}_x \vec{\boldsymbol{\nabla}}_x) \times \left(\frac{2}{\tilde{\hbar}} \sin\left(\frac{\tilde{\hbar}}{2} \overleftarrow{\boldsymbol{\nabla}}_x \vec{\boldsymbol{\nabla}}_u \right) - \overleftarrow{\boldsymbol{\nabla}}_x \vec{\boldsymbol{\nabla}}_u \right) f_{\mathrm{H}}(t_{\mathrm{ini}}) \tag{F3}$$

$$= -\frac{\tilde{\hbar}^2}{24} \Phi_{\mathrm{H}}(t_{\mathrm{ini}}) (\overleftarrow{\boldsymbol{\nabla}}_x \vec{\boldsymbol{\nabla}}_u)^3 f_{\mathrm{H}}(t_{\mathrm{ini}}) + \mathcal{O}({\tilde{\hbar}^2 {\sigma_x}^2}, \tilde{\hbar}^4) \tag{F4}$$

which we assumed to also hold at later times in (29) leading to the condition (32a). The smallest nonvanishing moment of the right-hand side of (F4) is for $n = 3$. Therefore, once the simulation is in the multistream regime and condition (37b) no longer applies, we can use the evolution equation of the third moment as an indicator of the goodness of the approximation of the coarse-grained Vlasov equation as in Sec. II E 4. If this condition does not hold, then $\partial_t f_{\mathrm{H}}$ is sourced by "quantum" corrections (F4) and the correspondence with the coarse-grained Vlasov equation is lost.

Similarly, from (4a) we see that

$$\partial_t(\bar{f}-f)_{\rm ini} = -\frac{{\sigma_u}^2}{a^2}\boldsymbol{\nabla}_x\boldsymbol{\nabla}_u\bar{f}(t_{\rm ini}) + \boldsymbol{\nabla}_x\bar{\Phi}(t_{\rm ini})(\exp({\sigma_x}^2\overleftarrow{\boldsymbol{\nabla}}_x\vec{\boldsymbol{\nabla}}_x)-1)\boldsymbol{\nabla}_u\bar{f}(t_{\rm ini}) \tag{F5}$$

$$= -\frac{{\sigma_u}^2}{a^2}\boldsymbol{\nabla}_x\boldsymbol{\nabla}_u\bar{f}(t_{\rm ini}) + {\sigma_x}^2\nabla_{x_i}\nabla_{x_j}\Phi_{\rm H}\nabla_{x_i}\nabla_{u_j}\bar{f}(t_{\rm ini}) + \mathcal{O}({\sigma_x}^4) \tag{F6}$$

leading to the condition (32b).

[1] P. J. E. Peebles, *The Large-Scale Structure of the Universe* (Princeton University Press, Princeton, NJ, 1980).
[2] V. Springel, S. D. M. White, A. Jenkins, C. S. Frenk, N. Yoshida, L. Gao, J. Navarro, R. Thacker, D. Croton, J. Helly, J. A. Peacock, S. Cole, P. Thomas, H. Couchman, A. Evrard, J. Colberg, and F. Pearce, Nature (London) **435**, 629 (2005).
[3] E. Tempel, R. S. Stoica, V. J. Martínez, L. J. Liivamägi, G. Castellan, and E. Saar, Mon. Not. R. Astron. Soc. **438**, 3465 (2014).
[4] N. E. Chisari and M. Zaldarriaga, Phys. Rev. D **83**, 123505 (2011).
[5] S. R. Green and R. M. Wald, Phys. Rev. D **85**, 063512 (2012).
[6] I. H. Gilbert, Astrophys. J. **152**, 1043 (1968).
[7] J. H. Jeans, Mon. Not. R. Astron. Soc. **76**, 70 (1915).
[8] R. Teyssier, Astron. Astrophys. **385**, 337 (2002).
[9] V. Springel, C. S. Frenk, and S. D. M. White, Nature (London) **440**, 1137 (2006).
[10] M. Boylan-Kolchin, V. Springel, S. D. M. White, A. Jenkins, and G. Lemson, Mon. Not. R. Astron. Soc. **398**, 1150 (2009).
[11] T. Abel, O. Hahn, and R. Kaehler, Mon. Not. R. Astron. Soc. **427**, 61 (2012).
[12] O. Hahn, T. Abel, and R. Kaehler, Mon. Not. R. Astron. Soc. **434**, 1171 (2013).
[13] P. Bertrand, N. van Tuan, M. Gros, B. Izrar, M. Feix, and J. Gutierrez, J. Plasma Phys. **23**, 401 (1980).
[14] L. M. Widrow and N. Kaiser, Astrophys. J. Lett. **416**, L71 (1993).
[15] G. Davies and L. M. Widrow, arXiv:astro-ph/9607133.
[16] P. Coles and K. Spencer, Mon. Not. R. Astron. Soc. **342**, 176 (2003).
[17] C. J. Short and P. Coles, J. Cosmol. Astropart. Phys. 12 (2006) 012.
[18] R. L. Guenther (1995).
[19] K. Husimi, Nippon Sugaku-Buturigakkwai Kizi Dai 3 Ki **22**, 264 (1940).
[20] T. Sousbie and S. Colombi, J. Comput. Phys. **321**, 644 (2016).
[21] K. Takahashi, Prog. Theor. Phys. Suppl. **98**, 109 (1989).
[22] R. T. Skodje, H. W. Rohrs, and J. VanBuskirk, Phys. Rev. A **40**, 2894 (1989).
[23] C. Uhlemann, M. Kopp, and T. Haugg, Phys. Rev. D **90**, 023517 (2014).
[24] M. Garny and T. Konstandin, arXiv:1710.04846.
[25] M. Schaller, C. Becker, O. Ruchayskiy, A. Boyarsky, and M. Shaposhnikov, Mon. Not. R. Astron. Soc. **442**, 3073 (2014).
[26] P. A. Markowich and N. J. Mauser, Math. Models Methods Appl. Sci. **03**, 109 (1993), http://www.worldscientific.com/doi/pdf/10.1142/S0218202593000072.
[27] P. Zhang, Y. Zheng, and N. J. Mauser, Commun. Pure Appl. Math. **55**, 582 (2002).
[28] Y. L. Klimontovich, *Statistical Theory of Non-equilibrium Processes in a Plasma*, Monographs in Natural Philosophy (Pergamon, New York, 1967).
[29] Y. Choquet-Bruhat, *General Relativity and the Einstein Equations, Oxford Mathematical Monographs* (Oxford University Press, New York, 2008).
[30] J. Binney and S. Tremaine, *Galactic Dynamics, chapter 4.8.3*, 2nd ed., Princeton Series in Astrophysics (Princeton University Press, Princteon, NJ, 2008).
[31] P. H. Chavanis, in *Dynamics and Thermodynamics of Systems with Long Range Interactions: Theory and Experiments*, American Institute of Physics Conference Series, Vol. 970, edited by A. Campa, A. Giansanti, G. Morigi, and F. S. Labini (Springer, New York, 2008), p. 39.
[32] V. I. Arnold, S. F. Shandarin, and I. B. Zeldovich, Geophys. Astrophys. Fluid Dyn. **20**, 111 (1982).
[33] S. Pueblas and R. Scoccimarro, Phys. Rev. D **80**, 043504 (2009).
[34] S. Shandarin, S. Habib, and K. Heitmann, Phys. Rev. D **85**, 083005 (2012).
[35] T. Abel, O. Hahn, and R. Kaehler, Mon. Not. R. Astron. Soc. **427**, 61 (2012).
[36] O. Hahn, R. E. Angulo, and T. Abel, Mon. Not. R. Astron. Soc. **454**, 3920 (2015).
[37] O. Hahn and R. E. Angulo, Mon. Not. R. Astron. Soc. **455**, 1115 (2016).
[38] J. W. Milnor, *Topology from the Differentiable Viewpoint* (University of Virginia, Charlottesville, VA, 1988).
[39] T. Buchert, in *Dark Matter in the Universe*, edited by S. Bonometto, J. R. Primack, and A. Provenzale (IOP, Amsterdam, 1996).
[40] K. Morawetz and R. Walke, Physica A (Amsterdam) **330**, 469 (2003).

[41] D. Lynden-Bell, Mon. Not. R. Astron. Soc. **136**, 101 (1967).
[42] E. R. Arriola and J. Soler, J. Stat. Phys. **103**, 1069 (2001).
[43] A. Suárez and P.-H. Chavanis, Phys. Rev. D **92**, 023510 (2015).
[44] E. Madelung, Z. Phys. **40**, 322 (1927).
[45] T. C. Wallstrom, Phys. Rev. A **49**, 1613 (1994).
[46] L. Hui, J. P. Ostriker, S. Tremaine, and E. Witten, Phys. Rev. D **95**, 043541 (2017).
[47] P. Mocz and S. Succi, Phys. Rev. E **91**, 053304 (2015).
[48] C. Trahan and R. Wyatt, *Quantum Dynamics with Trajectories: Introduction to Quantum Hydrodynamics*, Interdisciplinary Applied Mathematics (Springer, New York, 2005).
[49] H.-Y. Schive, T. Chiueh, and T. Broadhurst, Nat. Phys. **10**, 496 (2014).
[50] H.-Y. Schive, M.-H. Liao, T.-P. Woo, S.-K. Wong, T. Chiueh, T. Broadhurst, and W.-Y. P. Hwang, Phys. Rev. Lett. **113**, 261302 (2014).
[51] B. Schwabe, J. C. Niemeyer, and J. F. Engels, Phys. Rev. D **94**, 043513 (2016).
[52] D. W. Peaceman and H. H. Rachford, J. Soc. Ind. Appl. Math. **3**, 28 (1955).
[53] R. Harrison, I. Moroz, and K. P. Tod, Nonlinearity **16**, 101 (2003).
[54] A. Goldberg, H. M. Schey, and J. L. Schwartz, Am. J. Phys. **35**, 177 (1967).
[55] J.-T. Jia and Y.-L. Jiang, Numerical Algorithms **63**, 357 (2013).
[56] D. Layzer, Astrophys. J. **138**, 174 (1963).
[57] M. Joyce and F. S. Labini, Mon. Not. R. Astron. Soc. **429**, 1088 (2013).
[58] A. A. Klypin and S. F. Shandarin, Mon. Not. R. Astron. Soc. **204**, 891 (1983).
[59] J. Lesgourgues, arXiv:1104.2932.
[60] C. Pichon and F. Bernardeau, Astron. Astrophys. **343**, 663 (1999).
[61] S. Pueblas and R. Scoccimarro, Phys. Rev. D **80**, 043504 (2009).
[62] O. Hahn, R. E. Angulo, , and T. Abel, Mon. Not. R. Astron. Soc. **454**, 3920 (2015).
[63] S. S. L. Pitaevskii, *Bose-Einstein Condensation*, International series of monographs on physics 116 Oxford science publications (Clarendon, Oxford, 2003).
[64] D. Baumann, A. Nicolis, L. Senatore, and M. Zaldarriaga, J. Cosmol. Astropart. Phys. 07 (2012) 051.
[65] J. Katz, Mon. Not. R. Astron. Soc. **183**, 765 (1978).
[66] E. H. Lieb, in *Inequalities*, edited by M. Loss and M. B. Ruskai (Springer, Berlin, 1977), pp. 465–467.
[67] I. M. Moroz, R. Penrose, and P. Tod, Classical Quantum Gravity **15**, 2733 (1998).
[68] F. Staniscia, P. H. Chavanis, and G. de Ninno, Phys. Rev. E **83**, 051111 (2011).
[69] P. H. Chavanis, Int. J. Mod. Phys. B **20**, 3113 (2006).
[70] B.-B. Wei, New J. Phys. **18**, 113035 (2016).
[71] S. Floerchinger, M. Garny, N. Tetradis, and U. A. Wiedemann, J. Cosmol. Astropart. Phys. 01 (2017) 048.
[72] M. Kopp, C. Uhlemann, and T. Haugg, J. Cosmol. Astropart. Phys. 3 (2014) 018.
[73] M. Crocce, S. Pueblas, and R. Scoccimarro, Mon. Not. R. Astron. Soc. **373**, 369 (2006).
[74] T. Tatekawa and S. Mizuno, J. Cosmol. Astropart. Phys. 12 (2007) 014.
[75] O. Hahn and T. Abel, Mon. Not. R. Astron. Soc. **415**, 2101 (2011).
[76] Y. B. Zel'dovich, Astron. Astrophys. **5**, 84 (1970).
[77] N. Gouda and T. Nakamura, Prog. Theor. Phys. **81**, 633 (1989).
[78] T. Yano and N. Gouda, Astrophys. J. Suppl. Ser. **118**, 267 (1998).
[79] T. Tatekawa and K.-i. Maeda, Astrophys. J. **547**, 531 (2001).
[80] S. V. Tassev, J. Cosmol. Astropart. Phys. 10 (2011) 022.
[81] S. Colombi, Mon. Not. R. Astron. Soc. **446**, 2902 (2015).
[82] A. Taruya and S. Colombi, Mon. Not. R. Astron. Soc. **470**, 4858 (2017).
[83] S. N. Gurbatov, A. I. Saichev, and S. F. Shandarin, Mon. Not. R. Astron. Soc. **236**, 385 (1989).
[84] D. H. Weinberg and J. E. Gunn, Mon. Not. R. Astron. Soc. **247**, 260 (1990).
[85] S. N. Gurbatov, A. I. Saichev, and S. F. Shandarin, Physics **55**, 223 (2012).
[86] T. Buchert, A. Domínguez, and J. Pérez-Mercader, Astron. Astrophys. **349**, 343 (1999).
[87] P. Valageas, Astron. Astrophys. **526**, A67 (2011).
[88] P. Valageas, T. Nishimichi, and A. Taruya, Phys. Rev. D **87**, 083522 (2013).
[89] S. Tassev, M. Zaldarriaga, and D. J. Eisenstein, J. Cosmol. Astropart. Phys. 6 (2013) 036.
[90] S. Tassev, D. J. Eisenstein, B. D. Wandelt, and M. Zaldarriaga, arXiv:1502.07751.
[91] P. Monaco, T. Theuns, G. Taffoni, F. Governato, T. Quinn, and J. Stadel, Astrophys. J. **564**, 8 (2002).
[92] P. Monaco, T. Theuns, and G. Taffoni, Mon. Not. R. Astron. Soc. **331**, 587 (2002).
[93] P. McDonald and Z. Vlah, arXiv:1709.02834.